










Staring at the Shadows of Archaic Galaxies: Damped Ly α and Metal Absorbers toward a Young $z \sim 6$ Weak-line Quasar

IRHAM TAUFIK ANDIKA ^{1,2,3} KNUD JAHNKE ¹ EDUARDO BAÑADOS ¹ SARAH E. I. BOSMAN ¹
FREDERICK B. DAVIES ¹ ANNA-CHRISTINA EILERS ^{4,*} EMANUELE PAOLO FARINA ⁵ MASAFUSA ONOUE ^{1,6,7} AND
ARJEN VAN DER WEL ²

¹Max-Planck-Institut für Astronomie, Königstuhl 17, D-69117 Heidelberg, Germany

²Sterrenkundig Observatorium, Universiteit Gent, Krijgslaan 281 S9, 9000 Gent, Belgium

³International Max Planck Research School for Astronomy & Cosmic Physics at the University of Heidelberg

⁴MIT Kavli Institute for Astrophysics and Space Research, 77 Massachusetts Ave., Cambridge, MA 02139, USA

⁵Gemini Observatory, NSF's NOIRLab, 670 N A'ohoku Place, Hilo, Hawaii 96720, USA

⁶Kavli Institute for Astronomy and Astrophysics, Peking University, Beijing 100871, China

⁷Kavli Institute for the Physics and Mathematics of the Universe (WPI), University of Tokyo, Kashiwa, Chiba 277-8583, Japan

Abstract

We characterize the Ly α halo and absorption systems toward PSO J083+11, a unique $z = 6.3401$ weak-line quasar, using Gemini/GNIRS, Magellan/FIRE, and VLT/MUSE data. Strong absorptions by hydrogen and several metal lines (e.g., C II, Mg II, and O I) are discovered in the spectrum, which indicates the presence of: (i) a proximate sub-damped Ly α (sub-DLA) system at $z = 6.314$ and (ii) a Mg II absorber at $z = 2.2305$. To describe the observed damping wing signal, we model the Ly α absorption with a combination of a sub-DLA with the neutral hydrogen column density of $\log N_{\text{HI}} = 20.03 \pm 0.30 \text{ cm}^{-2}$ and absorption from the intergalactic medium with a neutral fraction of around 10%. The sub-DLA toward PSO J083+11 has an abundance ratio of $[\text{C}/\text{O}] = -0.04 \pm 0.33$ and metallicity of $[\text{O}/\text{H}] = -2.19 \pm 0.44$, similar to those of low-redshift metal-poor DLAs. These measurements suggest that the sub-DLA might truncate PSO J083+11's proximity zone size and complicate the quasar lifetime measurement. However, this quasar shows no sign of a Ly α halo in the MUSE datacube, where the estimated 1σ limit of surface brightness is $2.76 \times 10^{-18} \text{ erg s}^{-1} \text{ cm}^{-2} \text{ arcsec}^{-2}$ at aperture size of $1''$, or equivalent to a Ly α luminosity of $\leq 43.46 \text{ erg s}^{-1}$. This non-detection, while being only weak independent evidence on its own, is at least consistent with a young quasar scenario, as expected for a quasar with a short accretion timescale.

Keywords: cosmology: dark ages, reionization – galaxies: active, abundances – quasars: absorption lines, individual (PSO J083.8371+11.8482)

1. INTRODUCTION

Quasars are fueled by the matter accretion onto supermassive black holes (SMBHs). At high-redshifts, they can have SMBH masses of $\gtrsim 10^9 M_{\odot}$ as early as < 1 Gyr after the Big Bang (Bañados et al. 2018; Yang et al. 2020a; Wang et al. 2021). Hence, these quasars are excellent observational probes for understanding the build-up of the first SMBHs and the host galaxies, the early

structure formation, and the drivers of cosmic reionization (Mignoli et al. 2020; Bosman et al. 2021b; Pacucci & Loeb 2022). To date at $z > 6$, there are around 300 quasars discovered through various wide-field and deep-sky surveys (e.g., Fan et al. 2006; Willott et al. 2010; Mortlock et al. 2011; Venemans et al. 2015; Bañados et al. 2016; Mazzucchelli et al. 2017; Matsuoka et al. 2018; Reed et al. 2019; Yang et al. 2019; Wang et al. 2019; Pons et al. 2019; Matsuoka et al. 2022). Interestingly, tens of them were identified as so-called “young quasars” with estimated lifetimes of only $t_{\text{Q}} \sim 10^4\text{--}10^5$ years (Eilers et al. 2021). These young quasars create significant challenges since these luminous quasar life-

Corresponding author: Irham Taufik Andika
andika@mpia.de

* NASA Hubble Fellow

times are many times shorter than the typical time required for early SMBH growth ($t_Q \sim 10^6\text{--}10^9$ years; e.g., Khrykin et al. 2021; Worsack et al. 2021). The growth of these sources would require either: (i) direct collapse of massive seed black holes ($\gtrsim 10^4 M_\odot$; e.g., Begelman et al. 2006; Ferrara et al. 2014; Habouzit et al. 2016; Schauer et al. 2017; Dayal et al. 2019), (ii) nearly continuous accretion at (super)-Eddington limit onto lower-mass seeds ($\lesssim 10^2\text{--}10^3 M_\odot$; e.g., Ohsuga et al. 2005; Tanaka & Haiman 2009; Inayoshi et al. 2016), or (iii) the existence of radiatively inefficient accretions (e.g., Trakhtenbrot et al. 2017; Davies et al. 2019). Hence, both expanding the number of known quasars at this early epoch, the search specifically for young quasars, and detailed analyses of their properties are essential for a better understanding of early growth modes and the physics involved.

In our previous work we found a new weak emission line quasar at $z = 6.3401$, PSO J083.8371+11.8482 (hereafter PSO J083+11; Andika et al. 2020). Inferred from the small size of the proximity zone, we argued that this source clearly belongs to the young quasar population with a lifetime of only $t_Q \lesssim 10^4$ years for its latest luminous quasar phase. However, we found tentative evidence that the presence of a damped Ly α system (DLA; Wolfe et al. 2005) intervening our line of sight to the quasar might spectrally truncate PSO J083+11’s proximity zone, adding a complication to using the established quasar age measurement approach (Eilers et al. 2017). One aim of this paper is to rectify this situation and analyze the potential impact in-depth – as well as to add independent evidence for a young quasar age.

On the other hand, high- z DLAs themselves are of prime interest. They are excellent laboratories to examine the neutral-gas reservoirs which give rise to galaxies at cosmic dawn. These systems have the potential to be good tracers of the metal enrichment history by the first stars and their contribution to the universe’s reionization (e.g., Kulkarni et al. 2014; Ma et al. 2017). Moreover, metal-poor DLAs at high-redshifts are considered to be the progenitor of modern-day dwarf galaxies, which occupy the galaxy luminosity function at the faint end (Cooke et al. 2015). Finding and characterizing $z \gtrsim 6$ DLAs becomes extremely difficult due to increasing Ly α forest opacity (Eilers et al. 2018a; Bosman et al. 2018) of the intergalactic medium (IGM). Although metal absorbers are frequently detected at $z \gtrsim 6$, their hydrogen content is often unknown so that the absolute metal abundances can not be determined (e.g., Cooper et al. 2019). The currently best approach is to study “proximate” DLAs that reside close, in redshift, to a background quasar – i.e., within ~ 5000 km s $^{-1}$

– so that their Ly α damping wing absorptions extend into the forest-free quasar continuum, allowing us to estimate their neutral hydrogen column density (N_{HI}). To date, there are only four proximate DLAs found at $z \gtrsim 6$: SDSS J2310+1855 ($z_{\text{DLA}} = 5.939$; D’Odorico et al. 2018), PSO J056–16 ($z_{\text{DLA}} = 5.967$; Davies 2020), PSO J183+05 ($z_{\text{DLA}} = 6.404$; Bañados et al. 2019), and P007+04 (Farina et al., in preparation).

In this work, we present a study of the environment and absorption systems toward PSO J083+11. Using new integral-field unit (IFU) spectroscopic data from VLT/MUSE together with deep NIR spectroscopy presented in Andika et al. (2020): (i) we report on a newly-discovered $z = 6.314$ proximate absorber in the sightline of this quasar and constrain its effects on the quasar’s lifetime estimation; and (ii), we investigate the existence of a Ly α extended emission around the quasar itself that would add knowledge on the current quasar lifetime.

The structure of this paper is as follows. We start in Section 2 by describing data acquisition and reduction. Section 3 describes our metal absorption lines and Ly α damping wing measurements. After that, Section 4 presents our point-spread function modeling and methods to subtract out quasar continuum light to set limits on a Ly α halo around the quasar. Furthermore, we discuss the results in Section 5, including the elemental abundances of this proximate absorber and whether or not the absorber impacts the interpretation of the quasar’s observed proximity zone. We close with a summary of results and our conclusions in Section 6.

For all calculations, we use the flat Λ CDM cosmology, with $\Omega_\Lambda = 0.7$, $\Omega_m = 0.3$, and $H_0 = 70$ km s $^{-1}$ Mpc $^{-1}$. As a result, at $z = 6.3401$, the age of the universe is 0.852 Gyr, and the angular scale of $\theta = 1''$ corresponds to proper transverse separation of 5.5 kpc.

2. OBSERVATIONS AND DATA REDUCTION

As stated before, our goals are twofold. First, we want to make a deeper analysis of the quasar’s Ly α damping wing and its potential impact, and then also the physical properties of a potential intervening proximate absorber creating strong metal absorption lines, based on near-infrared (NIR) spectroscopy and modeling. The second goal is testing a prediction of the “young quasar” picture, which is the limited presence of extended Ly α emission near the central quasar. For this purpose, we obtained VLT/MUSE integral-field unit (IFU) spectroscopy to analyze the environment of PSO J083+11 spatially and spectrally resolved. The details of discovery and characterization of PSO J083+11 as well as HST and ALMA data and results were presented in Andika et al. (2020). Here we recap the main properties of the

initial and follow-up NIR spectroscopy, followed by a description of the VLT/MUSE IFU data.

2.1. Initial Observing Run with Magellan/FIRE

The first NIR spectroscopy of PSO J083+11 was obtained in January and February 2019 utilizing the 6.5m–Magellan/FIRE instrument (PI: R. Simcoe; [Simcoe et al. 2013](#)). The instrument was configured to the high-resolution echellette mode using the $0''.6$ slit to observe the target quasar for 5 hours. The resulting spectral data have a resolution in velocity space of $\sim 50 \text{ km s}^{-1}$, equivalent to a spectral resolution of $R \sim 6000$ within the wavelengths of 0.82–2.51 μm . Unfortunately, this observing run was conducted in suboptimal weather conditions, which results in a degraded signal-to-noise ratio (S/N). Nonetheless, the data are well suited for metal line diagnostic due to their spectral resolution, as shown below.

2.2. Gemini/GNIRS Near-infrared Spectroscopy

For proper characterization of the Ly α damping wing, we performed a second spectroscopic campaign to both create a high S/N – but lower resolution – spectrum in that region and at the same time calibrate-out instrument-specific effects at the long-wavelength end. This second run was performed on 20–22 March 2019 with 8060 seconds total time of integration on target using the 8.1m–Gemini-N/GNIRS (GN-2019A-FT-204, PI: M. Onoue). We chose the cross-dispersed mode to encompass a wavelength range of $\lambda_{\text{obs}} \sim 0.9\text{--}2.5 \mu\text{m}$ in the observed frame, using a 31.7 l/mm grating and a ‘short’ camera with $0''.15$ per pixel resolution. Using an aperture size of $0''.675$ slit resulted in a spectral resolution of $R \sim 750$. Single-frame exposure was 155 s long, and between exposures, a canonical ABBA pattern was used to reduce the noise from skylines. The observations were taken at an airmass range of $\sim 1.1\text{--}1.7$.

The details of the spectroscopic data reduction can be found in [Andika et al. \(2020\)](#). In summary, `PyPeIt`¹ ([Prochaska et al. 2020](#)) was used from cleaning the raw 2D spectrum – image differencing, flat-fielding, cosmic-ray removal, etc. – to producing the wavelength- and flux-calibrated 1D-spectrum. After that, contamination from telluric absorptions was corrected using `Molecfit`² ([Kausch et al. 2015](#); [Smette et al. 2015](#)). Finally, we utilized the dust map of [Green et al. \(2019\)](#) and extinction relation from [Gordon et al. \(2016\)](#) to correct reddening due to Galactic extinction.

¹ <https://pypeit.readthedocs.io/en/latest/>

² <https://www.eso.org/sci/software/pipelines/skytools/molecfit>

2.3. IFU Spectroscopy with VLT/MUSE

Specifically for the proximate absorber and environment analysis, we added red optical IFU spectroscopy for PSO J083+11 with MUSE at the 8.2m ESO VLT (0104.B-0665(A), PI: Andika), using the instrument’s wide-field mode. The resulting datacube has a spectral resolution of $R \sim 4000$ and covers the wavelength range of 0.47–0.93 μm . The quasar was observed for 3 hours, divided into five exposures of 2116 seconds, with shifts of $< 5''$ and rotations of 90° between exposures. Around the observed wavelength of Ly α the point-spread functions of bright stars in the field have a median width of $0''.5$. For data reduction, we used the MUSE DATA REDUCTION SOFTWARE version 2.6 ([Weilbacher et al. 2012, 2014](#)), complemented with a pipeline developed by [Farina et al. \(2019\)](#). The individual exposure was rescaled in flux before combining to avoid possible fluctuation of the photometry due to different weather conditions. Then the variance datacube was rescaled to match the observed background’s variance. Next, we improve the astrometric calibration by anchoring the sources to PAN-STARRS1 catalog ([Chambers et al. 2016](#)) and correct the Galactic reddening. After that, the contamination from night skylines was corrected utilizing the `Zurich Atmospheric Purge` software ([Soto et al. 2016](#)). Finally, the spectrum of the quasar is extracted from the datacube using a circular aperture with a radius of $0''.75$.

3. WHAT SHAPES THE LYMAN-ALPHA DAMPING WING?

The spectral data from MUSE, FIRE, and GNIRS allow us to investigate the presence of an absorber – e.g., (sub)-DLA or Lyman Limit System³ – close to the quasar that might influence the Ly α damping wing. In fact, we identified line-absorption that we associated with the Mg II $\lambda\lambda 2796, 2803$ doublet at $\lambda_{\text{obs}} = 20\,449.9, 20\,501.1 \text{ \AA}$; C II $\lambda 1334$ at $\lambda_{\text{obs}} = 9756.9 \text{ \AA}$; and a marginal detection of O I $\lambda 1302$ at $\lambda_{\text{obs}} = 9522.8 \text{ \AA}$. This is a strong indication of the proximate absorber presence located at $z = 6.314$. On the other hand, we could not confidently identify other associated metal line absorption like Si II, Al II, and Fe II that we would expect for a specifically strong DLA system. This indicates that the aforementioned proximate system is likely not a particularly strong absorber. In this section, we will constrain the quasar’s column density of neutral hydro-

³ Following [Cooper et al. \(2019\)](#), we employ the H I-based definition to classify the absorber as a Lyman Limit System ($\log N_{\text{HI}} \geq 17.2 \text{ cm}^{-2}$), sub-DLA ($19.0 < \log N_{\text{HI}} < 20.3 \text{ cm}^{-2}$), or DLA ($\log N_{\text{HI}} \geq 20.3 \text{ cm}^{-2}$).

gen to see whether the absorption from the proximate absorber is a dominant or significant factor impacting the Ly α damping wing detected in the PSO J083+11 spectrum.

As an aside, we also found independent line signatures of a strong Mg II absorber at a lower redshift – i.e., at $z = 2.2305$ – which we identified from the absorptions of Mg II $\lambda\lambda 2796, 2803$ doublet and Mg I $\lambda 2853$ at $\lambda_{\text{obs}} = 9032.5, 9055.1, \text{ and } 9216.6 \text{ \AA}$, respectively.

3.1. Metal Absorption Line Analysis

The spectra we utilized for metal absorption line measurements in this section are created based on the combined MUSE and FIRE data. As mentioned before, the FIRE data was taken during suboptimal weather conditions, which degrades its S/N. Hence, we first bin and convolve the FIRE spectrum to have a similar spectral resolution as MUSE (i.e., $R \sim 4000$), which as a consequence, the signal in the data also increases. Then, we stitch them together by keeping the data from MUSE at the observed wavelength of $\lambda_{\text{obs}} \leq 9300 \text{ \AA}$ while using the FIRE spectrum at $\lambda_{\text{obs}} > 9300 \text{ \AA}$.

To calculate the column densities of the metals presented in Figure 1, we needed to continuum normalize the PSO J083+11 spectrum first. We did this under the general assumption that the bulk of high-frequency structure were either absorption lines or was noise. With this assumption, the continuum was modeled using `QSmooth`⁴ (Ďurovčíková et al. 2020): this code first bins the spectrum with a running median of 50 data points to capture a first rough estimate of the main continuum and potential broad emission lines. It then constructs the spectrum’s upper envelope by performing a peak-finding procedure above the aforementioned running median and then interpolates the peaks. This envelope is almost independent of deep absorption features. It is then subtracted from the spectrum to create a first estimate of a continuum-subtracted spectrum – although while disregarding the impact of noise. `QSmooth` then applies the “Random Sample Consensus” regressor algorithm (Fischler & Bolles 1981) to search for statistical outlier in this intermediate subtracted spectrum. This process decides what is the inherent noise structure in the residual peak-subtracted continuum while rejecting most absorption lines. The “inliers” data points flagged by the algorithm – i.e., not being part of emission or absorption features – are interpolated and smoothed again by calculating a running median. This remaining struc-

ture is again removed, hence producing the final smooth flux fit of the spectrum.

Visual inspection is carried out on the continuum-normalized spectrum to check for the detection of potential other metal lines belonging to the very obvious Mg II at $z = 6.314$. The column densities were estimated straight from the spectral data by utilizing a Python code developed by Simcoe et al. (2020, see their Section 3). The code employs Markov Chain Monte Carlo (MCMC) samplers to explore the probability distributions of column density, the effect of saturation, and the degeneracies in the fitting parameters.

Before modeling, the user needs to provide a hierarchical absorption `Model` class. This class may consist of one or more fitting `Component` variables, representing absorbers with single or multiple-velocity clouds. Then, for each `Component` one needs to specify priors on redshift (z), thermal parameter (T) – which relates to temperature –, and turbulence parameter (b). Each `Component` contains several `Ion` children, where each `Ion` has a name (e.g., Mg II), a prior on column density (N), and an associated dictionary of `Transitions`. The `Transitions` themselves represent absorption lines and are defined based on their rest wavelengths and corresponding atomic data (Morton 2003).

The user then creates a `Model` class by entering `Component`, `Ion`, and `Transitions` along with suitable wavelength ranges to be modeled. In general, we fit regions within a velocity space of $\Delta v = \pm 125 \text{ km s}^{-1}$ around the center of each line, with some modifications for regions with higher noise. Note that the `Model` class contains a built-in method to generate Voigt profiles and convolve them with the appropriate instrumental resolution. This hierarchical workflow naturally fits the absorption component, which contains multiple ions and column densities, with a single value of z , b , or T . Furthermore, a single value of N can also be used for all transitions of an ion.

In our case, we employ a model using a single velocity component with column densities measured for 11 different ions containing 14 fitting parameters. This model and its corresponding priors are then supplied to the `emcee` software (Foreman-Mackey et al. 2013) to perform MCMC sampling and evaluate the posterior distributions of parameters. We note that flat priors are used for all input parameters, where $11 \leq \log N \leq 17$, $3 \leq \log T \leq 5$, and $2 \leq b \leq 100 \text{ km s}^{-1}$. The code is also able to estimate the upper limit of N because the posterior ranges from the prior lower limit to the maximum N allowed by the observed spectrum. In the case of undetected ions/lines, the z and b parameters are constrained by other ions in the same velocity component

⁴ <https://github.com/DominikaDu/QSmooth>

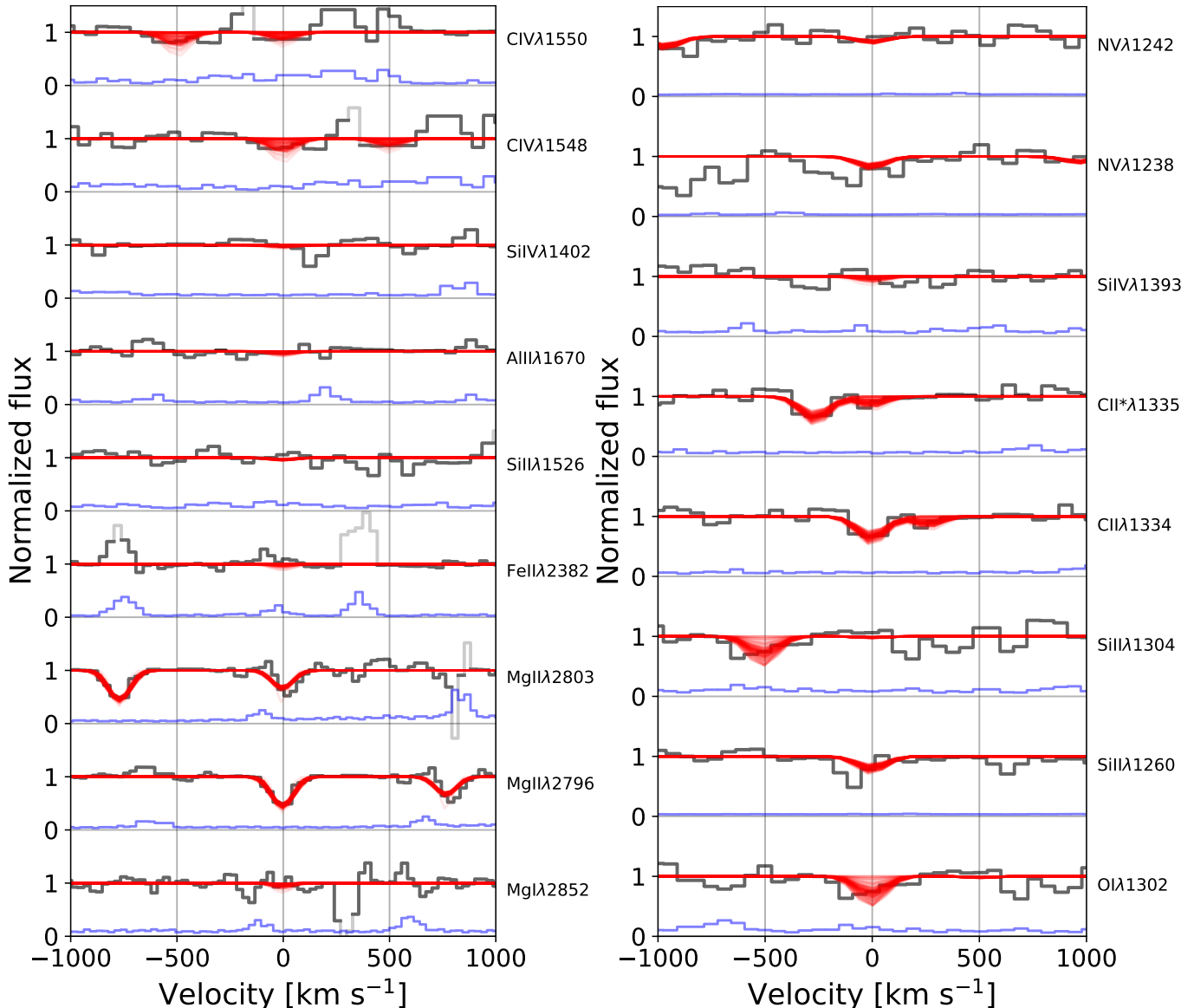


Figure 1. The velocity stack of the sub-DLA metal absorption lines at $z = 6.314$ observed in the continuum-normalized combined MUSE + FIRE spectrum. The data are shown as black lines with fitted models superposed in red. Note that the width of the red lines corresponds to the model uncertainty (see Section 3.1). Blue curves show a 1σ shot noise spectrum. We use grey lines to show the data in regions with high noise due to skylines. The absorptions from Mg II $\lambda\lambda 2796, 2803$ doublet and C II $\lambda 1334$ are clearly seen while there is only a marginal detection of O I $\lambda 1302$. Finally, the other associated metals like Si II, Al II, and Fe II which one would expect specifically for a strong absorber are not apparent in the spectrum.

with significant detections. The reported upper limits for non-detections mean the value below where 95% of the posterior distribution is found.

Figure 1 displays the models fitted to the MUSE + FIRE spectral data. A sample of 100 models chosen randomly based on the posterior distribution is shown with the red lines – the width of the red lines hence corresponds to the model uncertainty. The resulting fitting parameters are listed in Table 1, third column. Here, the reported abundances of C, O, Mg, Al, Si, and Fe are based on derived C II, O I, Mg II, Al II, Si II, and Fe II

column densities, respectively. We report a median and its corresponding 5% and 95% confidence levels. For undetected lines, we write a 95% upper limit. The posterior distributions of T , b , and metal column densities are reported in Appendix A. The model we prefer consists of a proximate absorber at $z = 6.314$ with thermal parameter of $\log T = 4.13 \pm 0.80$ K and turbulent parameter of $b = 59 \pm 20$ km s $^{-1}$. We note that most of the high-excitation lines such as C IV, Si IV, and N V are undetected within the sensitivity limits of our data. Therefore, the spectra with higher resolution and S/N

would be required to give better constraints on those ions.

As a piece of additional information, the previously identified Mg II absorber at lower redshift is best modeled with $z = 2.2305$, $\log T = 3.99 \pm 0.69$ K, and $b = 56 \pm 16$ km s⁻¹. This absorber also has column densities of $\log N_{\text{MgI}} = 12.86 \pm 0.07$ cm⁻² and $\log N_{\text{MgII}} = 13.75 \pm 0.04$ cm⁻².

3.2. Modeling the Lyman-alpha Line

How strong is the Ly α absorption from the intervening proximate absorber in the line of sight of PSO J083+11? To estimate this, we needed to model PSO J083+11's intrinsic Ly α emission first. This was done with two independent approaches: (i) stacking the spectra of lower-redshift quasars which have similar emission-line properties as PSO J083+11 to create a template (e.g., Bañados et al. 2019) and (ii) constructing a model based on principal component analysis (PCA; e.g., Davies et al. 2018a; Bosman et al. 2021a). For this analysis, we used the MUSE + GNIRS spectrum because although GNIRS has a lower resolution compared to FIRE, it gives better continuum S/N in the spectral data, which is useful for modeling the intrinsic quasar emission. The combined spectrum is then created by stitching $\lambda_{\text{obs}} \leq 9300$ Å MUSE data to $\lambda_{\text{obs}} > 9300$ Å GNIRS spectrum.

For the first approach, the construction of the empirical composite spectra based on low-redshift analogs relied on the knowledge that there is no significant quasar spectral evolution across redshifts (e.g., Shen et al. 2019). However, the $z \gtrsim 6$ quasars often show high ionization broad lines with more extreme velocity shifts compared to other $z < 5$ quasars at the same luminosity (Mazzucchelli et al. 2017; Meyer et al. 2019; Schindler et al. 2020). Nevertheless, a large number of Sloan Digital Sky Survey (SDSS; Abolfathi et al. 2018) quasars at lower- z provided a reasonable reference for creating a composite spectrum. Our method can be summarized as follow:

1. All quasars from the SDSS Data Release 14 Quasar Catalog (Pâris et al. 2018) flagged as non-broad absorption lines ($\text{BI_CIV} = 0$ km s⁻¹) were retrieved. We limited the selection to the redshifts of $2.0 < z < 2.5$ to include the Ly α , C IV, and Mg II lines in the spectra. This yielded 85,535 quasars.
2. The wavelength region around C IV was fit with a power-law to model the local continuum (for reference see Shen et al. 2011). Then, we estimated the C IV equivalent widths (EWs) based on the excess flux above the continuum over the wavelength range where C IV is expected. In this way

we selected quasars with a C IV EWs similar with PSO J083+11 ($\text{EW} \lesssim 5.8$ Å). These criteria left us with 23 quasar “analogs” with spectral properties similar to PSO J083+11.

3. The spectra of these analogs are smoothed by using QSmooth (Ďurovčiková et al. 2020, see above) to remove specifically noisy region and strong absorption lines in the spectra. We then normalized each of the 23 spectra at 1290 Å before averaging them into our final template.

The median composite spectrum and its 1σ dispersion are presented in Figure 2. The composite spectrum matches most of the traits observed in the PSO J083+11 spectrum and predicts an intrinsically weak Ly α line.

For the second approach, we used PCA of lower redshift quasar spectra to predict the strength and shape of Ly α using strong correlations between Ly α emission and other rest-frame ultraviolet broad emission lines that are known to be present (Francis et al. 1992; Yip et al. 2004; Suzuki 2006). This makes PCA approach to also predict the blue part ($\lambda_{\text{rest}} < 1290$ Å) of the quasar spectrum – including Ly α – based only on its red part ($\lambda_{\text{rest}} \geq 1290$ Å; e.g., Suzuki 2006; Pâris et al. 2011; Davies et al. 2018a,b). We refer to Bosman et al. (2021a) for the details on the PCA model construction that we used. In brief, our training set consisted of ~ 4000 quasars again retrieved from the SDSS DR14 quasar catalog (Pâris et al. 2018). Then, PCA decomposition was performed to capture 70–80% of the total spectral variance with a linear combination of only 10 and 6 principal components for the red- and blue-side spectra, respectively. After that, we calculated a projection matrix that connects the coefficients from the red-side to those on the blue-side of the spectrum. Thus, the blue side spectrum can be predicted based on the projected blue-side coefficients and the associated spectral template. The PCA model for PSO J083+11 is presented in Figure 2. It predicts a weaker Ly α and provides a formally better match to the observed data than the constructed lower- z “analogs”-template, although both models are still consistent with each other within the estimated uncertainties. Compared to the composite spectrum based on the low-redshift quasar analogs, however, PCA considers not only C IV but implicitly also all broad lines characteristics, which makes it in principle superior given the extra information it uses. Therefore, we utilize the PCA model for the remainder of the analysis to take advantage of its well-quantified uncertainties.

This then allowed us to model the absorption in the Ly α region. A Voigt model centered at $z = 6.314$ was fitted to the observed damping wing in the PSO J083+11

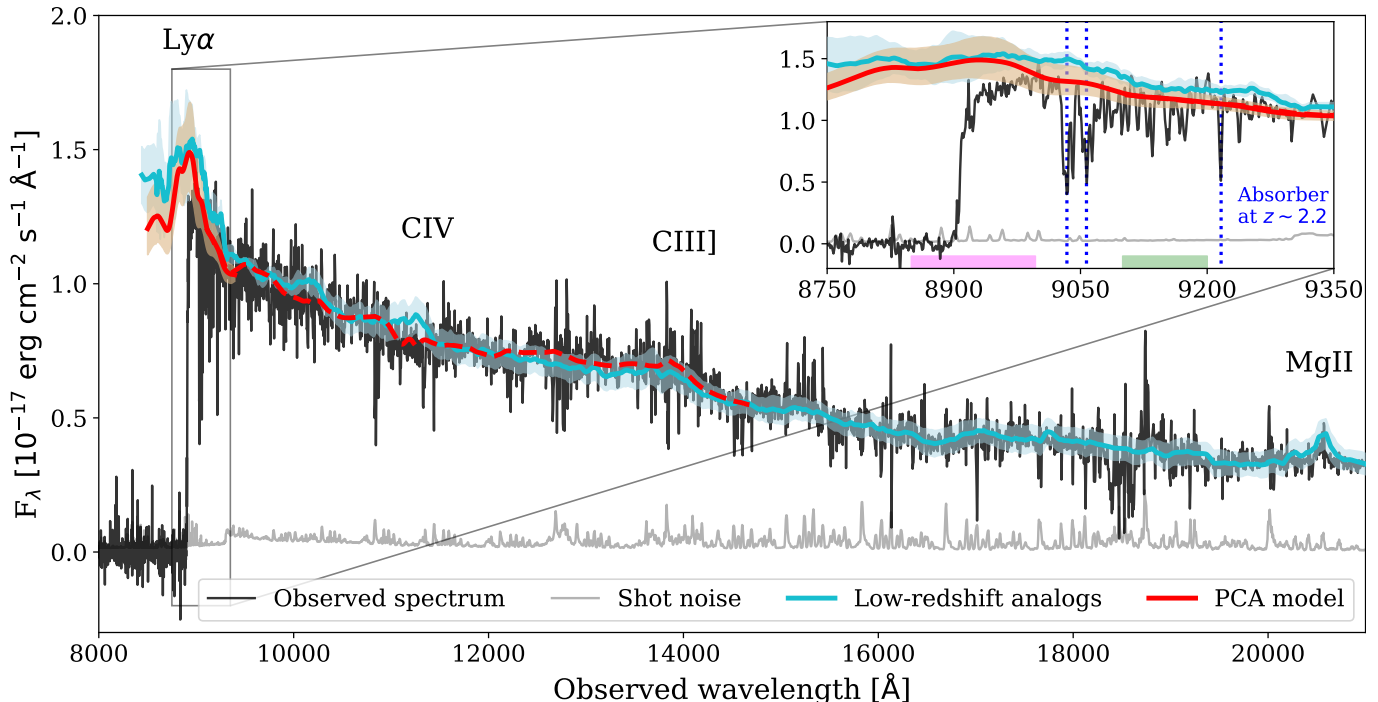


Figure 2. The MUSE + GNIRS spectrum of PSO J083+11 (black line) and its associated shot noise (grey line). The median composite spectrum of the low-redshift quasar analogs is shown as a cyan line with the 1σ dispersion around the median as a light blue region. The composite spectrum gives a decent fit to the main features observed in the PSO J083+11 spectrum redward of the Ly α emission. On the other hand, the PCA model to better predict the blue-side of the quasar spectrum and its 1σ dispersion are denoted with the red line and shaded region, respectively. The wavelength range and spectrum used in the PCA fit to predict Ly α is shown with the red dashed line. The inset figure shows the zoom-in to the region around Ly α . The Mg II $\lambda\lambda 2796, 2803$ doublet and Mg I $\lambda 2853$ absorptions at $z = 2.2305$ are marked with blue dotted lines. The wavelength ranges highlighted with magenta ($\lambda_{\text{obs}} = 8850\text{--}8997$ Å) and green ($\lambda_{\text{obs}} = 9100\text{--}9200$ Å) colors are the region of interest for creating the Ly α pseudo-narrowband and continuum images, respectively.

spectrum – we chose this proximate absorber redshift based on the location of metal absorption lines (see Section 3.1). Optimization using least-squares yielded a best-fit value of $\log N_{\text{HI}} = 20.11 \pm 0.30$ cm $^{-2}$. An uncertainty of range in N_{HI} was estimated by over-plotting Voigt profiles, modifying the column density input to determine the allowed range by the observed spectrum and the continuum model. This approach to making a subjective visual estimate of the uncertainty in the absorption profile is currently the standard methodology in the field (e.g., Bañados et al. 2019), because it is difficult to quantify the full set of errors from continuum mismatch, unaccounted-for absorption lines, and shot noise. Hence making a statement of the goodness of fit just from χ^2 alone would create an unrealistically small range of likely consistent N_{HI} values. Note that although a single Voigt profile already gives a reasonable fit overall, we want to explore an alternative model to test how much the PSO J083+11’s proximity zone is truncated due to the presence of the aforementioned proximate absorber.

Another mechanism that is likely involved and that influences the damping wing is the hydrogen absorption in the IGM with a neutral fraction of $\bar{x}_{\text{HI}} > 10\%$ (Miralda-Escudé 1998; Bañados et al. 2019). Following the formalism of Miralda-Escudé (1998), we tried to model the IGM damping wing presuming a constant neutral fraction from quasar’s proximity zone at redshift $z = z_s$ to $z = 5.5$, while being entirely ionized around $z \lesssim 5.5$. By definition, the proximity zone is the physical radius at which the transmitted flux drops to 10%, which for PSO J083+11 is equivalent to $R_p = 1.17 \pm 0.32$ pMpc (Andika et al. 2020).

As discussed by Bañados et al. (2019, see their Appendix A.2), fitting the data with an IGM + DLA combined model with three free parameters (\bar{x}_{HI} , N_{HI} , and R_p) would give a highly degenerated result. To reduce this dimensionality problem, we stepped through several IGM damping wing appearances using a grid of constant \bar{x}_{HI} and R_p . Then, we fitted the DLA Voigt profile to the already attenuated continuum. The result is that indeed a joint model of IGM plus DLA always gives a slightly better, although not significant,

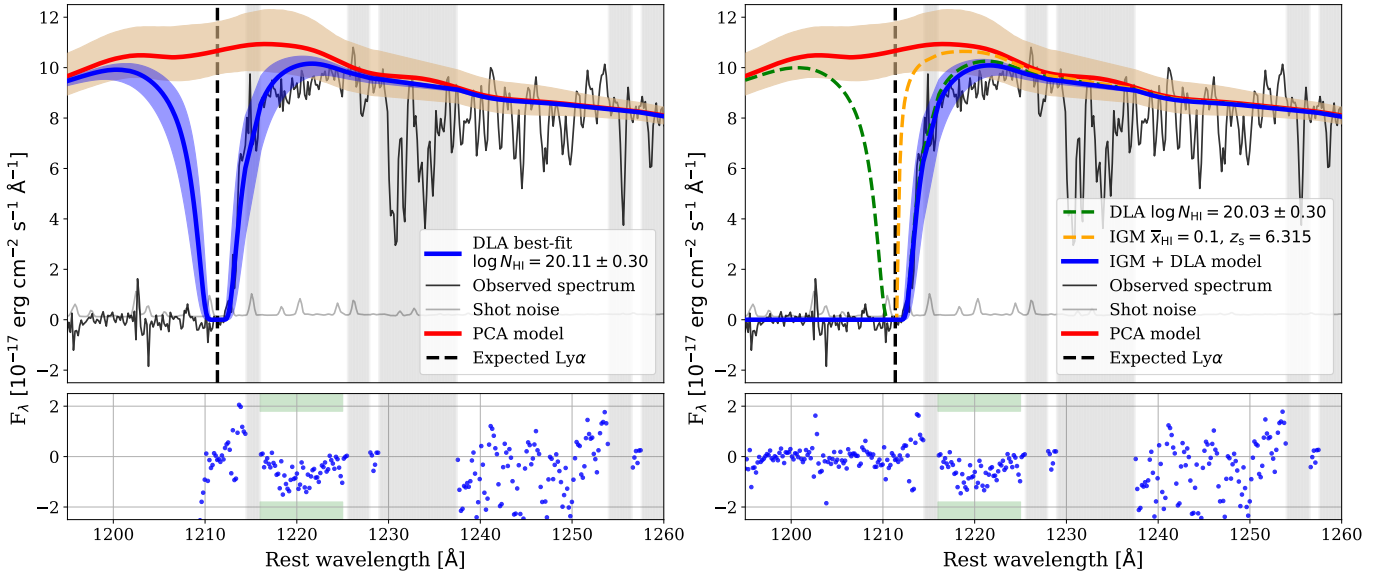


Figure 3. The spectrum of PSO J083+11 (black line), shot noise (grey line), and the associated PCA model (red line and shaded region) around the wavelength region where the quasar’s Ly α emission is expected. The *left panel* shows the absorption from a $z = 6.314$ sub-DLA with a hydrogen column density of $\log N_{\text{HI}} = 20.11 \pm 0.30 \text{ cm}^{-2}$ (blue line and shaded region). Even though it already gives a good fit, we explore an alternative model to test how much the PSO J083+11’s proximity zone is truncated due to the presence of the aforementioned sub-DLA. The *right panel* presents a joint model where we incorporated attenuation due to an IGM with $\bar{x}_{\text{HI}} = 0.1$ (orange dashed line) and sub-DLA with $\log N_{\text{HI}} = 20.03 \pm 0.30 \text{ cm}^{-2}$ (green dashed line). This joint IGM + DLA model (blue line and shaded region) reconstructs the data at $\lambda = 1216\text{--}1225 \text{ \AA}$ slightly better, although not significant (see wavelengths marked with green). The residual of the fits (blue circles) and masked wavelengths to avoid strong absorption lines or regions with large uncertainty in the sky-subtraction (grey shaded area) are also presented in the figure. See Appendix C for the impact of other \bar{x}_{HI} values.

fit than using only a DLA, especially at $\lambda = 1216\text{--}1225 \text{ \AA}$ (see Figure 3). For the Ly α emission line model reconstructed with PCA, we found that the allowed DLA profiles that can produce the observed damping wing have $\log N_{\text{HI}} = 20.03\text{--}19.73 \text{ cm}^{-2}$ for an IGM that is 10–50% neutral. Consequently, this exercise also gives the proximity zone size that is allowed by the observed spectrum, i.e., $R_p \gtrsim 1.35 \text{ pMpc}$. Note that we can only calculate the lower limit of R_p because if the quasar’s proximity zone extends beyond the DLA location (i.e., $z_s < z_{\text{DLA}}$), it will be hidden from the observer and poorly constrained due to the blockage by the DLA cloud. Furthermore, the proximity zone size will no longer be sensitive to quasar lifetime, and hence, another independent diagnostic for measuring the age would be required. See Appendix C for a display of how different combinations of neutral fractions and z_s affect the damping wing model.

For the remainder of the analysis, we choose our preferred model, which is a 10% neutral IGM and corresponds to the best-fit DLA Voigt profile of $\log N_{\text{HI}} = 20.03 \pm 0.30 \text{ cm}^{-2}$. This value encompasses the best-fit N_{HI} for all cases where $\bar{x}_{\text{HI}} \leq 50\%$. Moreover, the values of the $\bar{x}_{\text{HI}} > 50\%$ seem unlikely because the best-fit damping wing profiles systematically underestimate

the observed fluxes around $\lambda = 1216\text{--}1225 \text{ \AA}$. Selection of this model was also motivated by the fact that IGM with $\bar{x}_{\text{HI}} \gtrsim 0.4$ has only been found at higher redshifts (e.g., Davies et al. 2018b; Wang et al. 2020). In addition, Yang et al. (2020b) also derive a lower limit for the neutral fraction at $z \sim 6$, which is $\bar{x}_{\text{HI}} \gtrsim 10^{-4}$. This value was inferred based on the measurements of Ly α effective optical depth and hydrodynamical simulations assuming a uniform ultraviolet background. At the same time, Yang et al. (2020b) also note that their model does not rule out a possibility of $\bar{x}_{\text{HI}} \sim 0.1\text{--}0.2$, but not much beyond that.

For completeness, we also attempt to model Ly α damping wing using MUSE and the lower-quality FIRE spectra, presented in Appendix B. The PCA model, in this case, is more strongly impacted by telluric line residuals and less by intrinsic features aside from the general quasar spectral slope. This results in spurious, much higher prediction of Ly α line flux, in turn requiring an unphysical neutral fraction of $\bar{x}_{\text{HI}} \geq 80\%$. Hence we do not consider FIRE to add robust and trustworthy independent information to this analysis.

4. CONSTRAINTS ON A LYMAN-ALPHA HALO

To find alternative support for the young quasar contention, we exploited MUSE data for constraining the extension of the Ly α halo around the PSO J083+11. Previously discovered Ly α halos around early quasars (Farina et al. 2019) guide our expectation on the potential extent ($\lesssim 30$ pkpc) and luminosity ($\log L_{\text{Ly}\alpha} \sim 42 - 44$ erg s $^{-1}$). These parameters set a clear need for a removal of the quasar continuum point source light, smeared out by the VLT/MUSE $\sim 0''.5$ PSF, before a search for the halo can be carried out.

4.1. Quasar Point Source Modeling and Subtraction

For all practical purposes, the quasar’s accretion disk can be considered as a point source in the rest-frame ultraviolet and optical. For any given IFU wavelength, the point-spread function (PSF) can be constructed based on neighboring bright stars in the frame, or – for regions of line emission – from adjacent spectral regions of quasar continuum (Farina et al. 2017).

Using Drake et al. (2019) as a reference, we modeled the PSF from data in the following steps. Several spectral layers in the MUSE cube containing quasar’s continuum were chosen and collapsed to produce a local PSF model. Ideally, we would need to include a spectral range as wide as possible to increase the S/N. However, there is on one side contamination from night sky emissions across the wavelength of interest that modify noise properties of the adjacent wavelength layers, resulting in S/N degradation. On the other side, the PSF is chromatic due to wavelength-dependent diffraction in the air of different densities, requiring choosing wavelength ranges for PSF construction close to the wavelength range for which the PSF is constructed. Therefore, we collapsed the wavelength layers of the region $\lambda_{\text{obs}} = 9100\text{--}9200$ Å where contamination is minimal, quasar continuum has high enough S/N while staying within a few percent distances to the Ly α wavelength (see the inset of Figure 2).

With this PSF in hand, we subtract the quasar point source by normalizing the PSF model to match each of the MUSE cube wavelength layers within the Ly α spectral region, i.e., at $\lambda_{\text{obs}} = 8850\text{--}8997$ Å. For this, we simply scale the fluxes measured within an aperture radius of two spatial pixels ($0''.4$, at an angular resolution of $0''.3\text{--}0''.4$ for the MUSE data), assuming that this central region is massively dominated by the unresolved quasar’s emission (e.g., Farina et al. 2017, 2019). Finally, subtracting the scaled PSF model cube from the Ly α cube layer gave us an entire quasar nucleus-subtracted data cube containing an extended, i.e., not point-source, flux.

4.2. The Non-detection of a Lyman-alpha Halo

We show the MUSE-based images of PSO J083+11 in Figure 4. Both Ly α - and continuum-spectrum of the quasar are extracted using a radius of $0''.75$ as showed by the black dotted circle in the images. The left panel presents the constructed pseudo-narrowband image centered on the Ly α line, the middle image the constructed continuum image we used as a quasar PSF model. The quasar point source subtracted image is shown in the right panel, which is equivalent to the continuum image subtracted from the Ly α -image on the left.

The image itself does not show an obvious extended halo of high surface brightness. To test this down to fainter surface brightness levels, we followed Drake et al. (2019) and performed aperture photometry with multiple radii to construct an azimuthally-averaged radial light profile of potential extended Ly α emission (Figure 5). The estimated 1σ surface brightness limit of the quasar continuum-subtracted pseudo-narrowband image is 2.76×10^{-18} erg s $^{-1}$ cm $^{-2}$ arcsec $^{-2}$, corresponding to a Ly α luminosity upper limit of $\log L_{\text{Ly}\alpha} \lesssim 43.46$ erg s $^{-1}$ at $1''$ aperture radius. In addition, we also found a marginal halo flux detection within a $0''.6$ aperture radius, but there are no evident extended Ly α emissions beyond this radius.

Previous studies discovered that the Ly α halo luminosity does not depend directly on the quasar’s instantaneous ionizing flux, which can be probed with the absolute magnitude at 1450 Å (M_{1450} ; e.g., Arrigoni Battaia et al. 2019; Drake et al. 2019). In other words, circumgalactic medium properties, including ionization state, temperature, and density, play a more important role in producing the Ly α halo emission (see e.g., Mackenzie et al. 2021). Out of 31 quasars studied by Farina et al. (2019), 19 of them have absolute magnitudes comparable to PSO J083+11, i.e., $-26 \lesssim M_{1450} \lesssim 27$. To make a direct comparison with the depth of Farina et al. (2019) data, we estimate the surface brightness limit of our MUSE image following their prescription. The calculation is done by collapsing five wavelength channels – or equivalent to a total of 6.25 Å – around the expected location of PSO J083+11’s Ly α emission. Subsequently, we obtain a 5σ surface brightness limit of 0.29×10^{-17} erg s $^{-1}$ cm $^{-2}$ arcsec $^{-2}$ for a circular aperture with a radius of $1''$. This means that our data is comparable with the depth of their samples – i.e., surface brightness limits of ranging from 0.1 to 1.1×10^{-17} erg s $^{-1}$ cm $^{-2}$ arcsec $^{-2}$.

Intriguingly, of the 19 quasars in the Farina et al. (2019) subsample, ten show halos with luminosities ranging from $\log L_{\text{Ly}\alpha} = 42.9$ to 44.3 erg s $^{-1}$ while the other nine quasars do not show any signs of extended

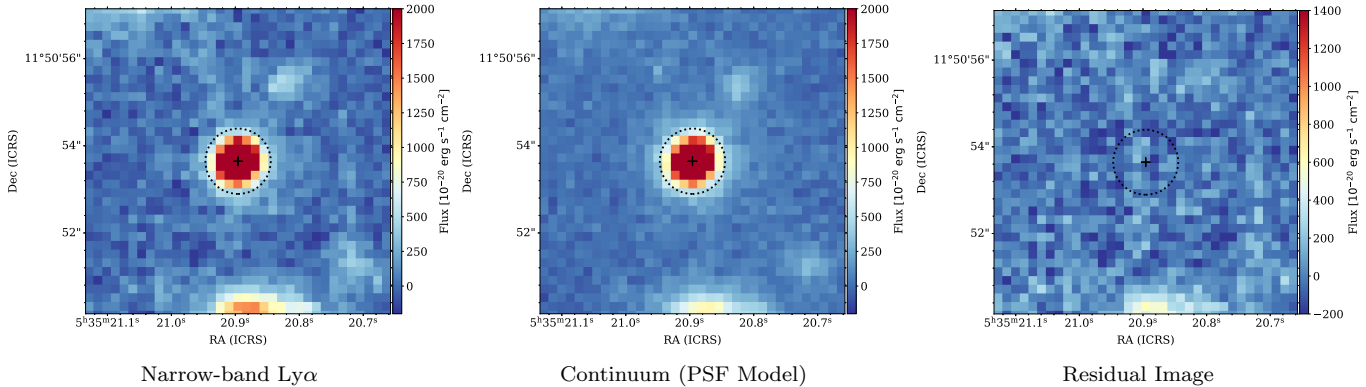


Figure 4. The pseudo-narrowband images of PSO J083+11 created based on the MUSE data. The black dotted circles mark an aperture with a size of $0''.75$ used for extracting the quasar spectrum. In the *left panel*, we show the pseudo-narrowband image centered on the expected Ly α emission wavelength ($\lambda_{\text{obs}} = 8850\text{--}8997$ Å) as highlighted by the magenta region of the spectrum in the inset of Figure 2. The continuum, and hence point-source image, constructed by collapsing data cube wavelength layers around the quasar continuum emission, is shown in the *middle panel*. The wavelength range ($\lambda_{\text{obs}} = 9100\text{--}9200$ Å) combined into this image is denoted in green in the inset of Figure 2. Finally, the *right panel* shows the pseudo-narrowband image centered on the Ly α line after removing the quasar point source with the PSF subtraction procedure explained in Section 4.1. There is no obvious detection of Ly α halo as seen in the point source-subtracted residual image. As a side note, the bright emission to the south of the central quasar comes from a foreground galaxy located at $z \approx 0.29$.

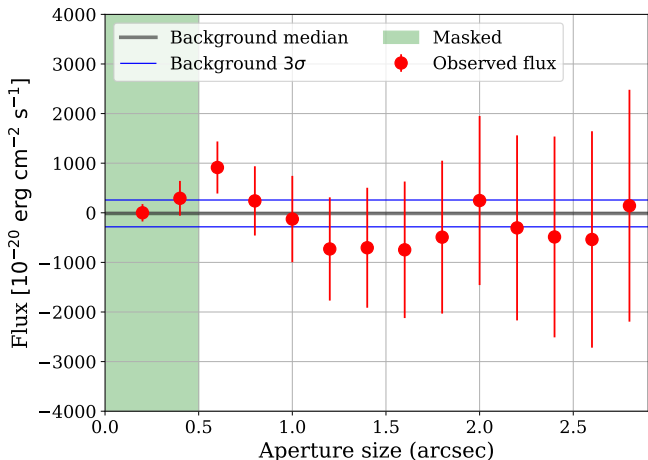


Figure 5. The azimuthally averaged radial light profile of PSO J083+11’s Ly α emission measured from the PSF-subtracted pseudo-narrowband image. Tentative detection of the halo flux within a $0''.6$ aperture radius is observed, but there are no apparent extended Ly α emissions beyond this radius.

Ly α emission. In other words, at the current depth of our MUSE data, there is a $\sim 50\%$ chance that the PSO J083+11’s Ly α halo is intrinsically non-existent and a 50% probability that the halo exists but is below our detection limit. However, if we wanted to decrease the current surface brightness limit by a factor of two, around ten hours of additional observing time with MUSE will be needed – both for PSO J083+11 as well as each of the nine comparison quasars from Farina et al. We also note that there are two notably fainter quasars, J2329–0301 ($M_{1450} = -25.19$) and

J2228+0110 ($M_{1450} = -24.47$), which show halos with luminosity of at least $\log \text{Ly}\alpha > 43.7$ erg s $^{-1}$ (Farina et al. 2019). It is also interesting to note that none of the three known young quasars with estimated lifetimes of only $t_Q \sim 10^3\text{--}10^4$ years – i.e., J2229+1457 ($M_{1450} = -24.72$), J0100+2802 ($M_{1450} = -29.09$), and J2100–1715 ($M_{1450} = -25.50$) – show presence of extended Ly α halo (Farina et al. 2019; Davies et al. 2020b; Eilers et al. 2021). In the case of PSO J083+11, this might indicate that there is not enough Ly α diffuse gas surrounding quasar to emit a halo, or, alternatively, ionizing light from the young quasar phase has not had time to travel far enough. Note that the light travel time for a halo with a size of $0''.6$, or equivalent to 3.32 pkpc, corresponds to $\sim 10^4$ years.

5. DISCUSSION

5.1. Elemental Abundance Ratios

The new $z = 6.314$ proximate absorber presented here resembles the low-ionization systems characterized by Cooper et al. (2019) and Simcoe et al. (2020), where large column densities of elements like Mg II, C II, and O I are observed but we find no absorptions from highly ionized elements such as Si IV or C IV. In our case, we found $\log N_{\text{MgII}} = 13.33 \pm 0.03$ cm $^{-2}$, $\log N_{\text{CII}} = 14.23 \pm 0.09$ cm $^{-2}$, $\log N_{\text{OI}} = 14.53 \pm 0.32$ cm $^{-2}$, $\log N_{\text{SiIV}} < 12.91$ cm $^{-2}$, and $\log N_{\text{CIV}} < 13.87$ cm $^{-2}$. This source also differs from the typical lower-redshift DLAs ($2 \lesssim z \lesssim 4$), which are likely to have the associated C IV, but, for the given redshift, this is not unexpected due to a decreasing rate of high-ionization absorbers at $z \gtrsim 5$

Table 1. Elemental abundances of the $z = 6.314$ sub-DLA in the line of sight of PSO J083+11.

X	$\log \epsilon(X)_\odot^a$	$\log N_X \text{ (cm}^{-2}\text{)}$	[X/H]
H	12.00	20.03 ± 0.30	–
C	8.43	14.23 ± 0.09	-2.23 ± 0.31
O	8.69	14.53 ± 0.32	-2.19 ± 0.44
Mg	7.53	13.33 ± 0.03	-2.23 ± 0.30
Al	6.43	< 12.15	< -2.31
Si	7.51	< 13.16	< -2.38
Fe	7.45	< 12.67	< -2.81

NOTE—The calculated relative abundances do not include dust depletion and ionization corrections. The elemental ratios are relative to the solar abundances, i.e., $[X/Y] = \log(N_X/N_Y) - \log(N_X/N_Y)_\odot$.

^aThe definition is $\log \epsilon(X)_\odot = 12 + \log(N_X/N_H)_\odot$.

(Cooper et al. 2019). On the other hand, the non-detection of Mg I with $\log N_{\text{MgI}} < 11.98 \text{ cm}^{-2}$ implies some degree of ionization from the radiation field of massive stars in the far-ultraviolet regime (Simcoe et al. 2020). In addition, we also could not find other associated metal line absorptions like Si II, Al II, and Fe II – i.e., $\log N_{\text{SiII}} < 13.16 \text{ cm}^{-2}$, $\log N_{\text{AlII}} < 12.15 \text{ cm}^{-2}$, and $\log N_{\text{FeII}} < 12.67 \text{ cm}^{-2}$ – that we would expect for a specifically strong DLA system.

We report the element ratios relative to the solar abundances (Asplund et al. 2009) in Table 1. For O and C, we derive the solar abundances based on the photospheric values while for other elements we utilize the meteoritic values (see e.g., Bañados et al. 2019). Note that the observed $\log N_{\text{HI}} = 20.03 \pm 0.30 \text{ cm}^{-2}$ means that this cloud is more similar to a sub-DLA system ($19.0 < \log N_{\text{HI}} < 20.3 \text{ cm}^{-2}$; Milutinovic et al. 2010; Cooper et al. 2019) and the actual elemental abundances might need ionization and dust depletion corrections with a total factor of $\sim 0.0\text{--}0.7$ dex. (e.g., Milutinovic et al. 2010; Quiret et al. 2016; Berg et al. 2021).

There is a known stellar relation that the [C/O] element ratio is linearly increasing with metallicity in the range $-0.5 < [\text{C}/\text{O}] < 0.5$ and $[\text{O}/\text{H}] > -1$. An explanation is an increase in carbon production by rotating massive stars – which also increases with metallicity – plus a delayed carbon production from stars with lower masses (Akerman et al. 2004). On the other hand, at $[\text{O}/\text{H}] \lesssim -1$, it there is an opposite trend observed in metal-poor DLAs (Cooke et al. 2017; Bañados et al. 2019) and metal-poor stars (Akerman

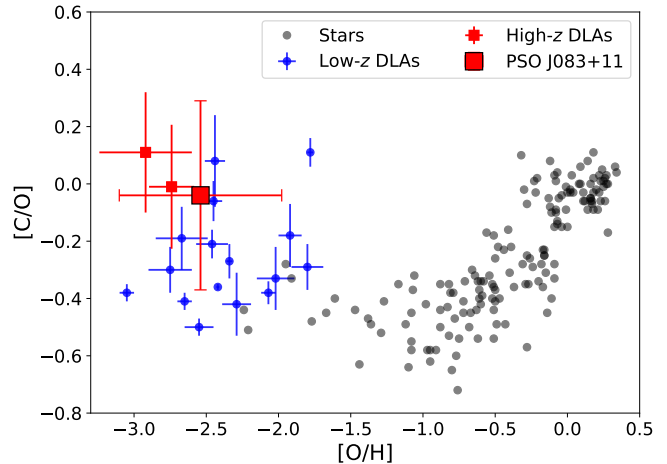


Figure 6. The relation between metallicity $[\text{O}/\text{H}]$ and chemical evolution of $[\text{C}/\text{O}]$. Measurements for Milky Way stars taken from Fabbian et al. (2009) and Nissen et al. (2014) are marked as grey circles, while low-redshift DLAs ($2 \lesssim z \lesssim 4$) from Cooke et al. (2017) are denoted with blue circles. The $z \gtrsim 6$ metal-poor DLAs from Bañados et al. (2019) and D’Odorico et al. (2018) are shown with red squares. Specific for the sub-DLA toward PSO J083+11, we show a corrected metallicity where we adopt a correction factor of 0.35 ± 0.35 dex (see text) to account for ionization and depletion effects. Consequently, this changes the measured $[\text{O}/\text{H}]$ from -2.19 ± 0.44 to -2.54 ± 0.56 .

et al. 2004; Fabbian et al. 2009) – i.e., an actual increases of $[\text{C}/\text{O}]$. PSO J083+11 seems to follow this empirical trend, showing similar $[\text{C}/\text{O}]$ abundance and $[\text{O}/\text{H}]$ metallicity compared to other metal-poor DLAs (see the red square in Figure 6). The calculated abundance is $[\text{C}/\text{O}] = -0.04 \pm 0.33$ while the derived metallicity is $[\text{O}/\text{H}] = -2.19 \pm 0.44$. We refer the reader to Cooke et al. (2011) and Ma et al. (2017) for further references on the possible formation scenarios that could clarify the chemical composition of the DLAs.

5.2. Is the Presence of a DLA Truncating PSO J083+11 Proximity Zone?

Around the end of reionization epoch ($z \sim 6$) there are regions of the IGM with partially still neutral hydrogen components, suppressing all photon transmission blue-ward of the $\text{Ly}\alpha$ wavelength (e.g. Gunn & Peterson 1965). However, a luminous quasar might be capable to ionize the adjacent medium with its intense radiation, producing a bubble of enhanced transmission in the nearby $\text{Ly}\alpha$ forest titled as the proximity zone (e.g., Fan et al. 2006; Eilers et al. 2017).

In Andika et al. (2020), we argued that PSO J083+11 is having a small size of proximity zone in absolute terms ($R_p = 1.17 \pm 0.32 \text{ pMpc}$) due to a limited lifetime of unobscured accretion, and hence unobscured emission

into its environment ($t_Q = 10^{3.4 \pm 0.7}$ years; i.e., a young quasar). This measured proximity zone is substantially below the size for typical $z \sim 6$ quasars with similar luminosity as PSO J083+11, i.e., $R_{p, \text{typical}} \sim 4$ pMpc (Eilers et al. 2020, see their Figure 7). Correspondingly, the accretion lifetime itself can be inferred from the quasar’s proximity zone size, where smaller sizes correspond to a younger lifetime (Eilers et al. 2018b; Davies et al. 2020a; Eilers et al. 2020; Chen & Gnedin 2021). However, due to the limitation of our earlier initial data, we could not constrain whether or not the proximate absorber might play a significant role in blocking ionizing radiation from the central quasar to the IGM – potentially making the proximity zone measurement inaccurate.

We now improved on this after locating and characterizing the proximate sub-DLA system at $z = 6.314$ with a column density of neutral hydrogen of $\log N_{\text{HI}} = 20.03 \pm 0.30 \text{ cm}^{-2}$. In Section 3.2, we stepped over a range of IGM damping wing shapes using a grid of constant \bar{x}_{HI} and proximity zone sizes, then fitted a Voigt profile as the sub-DLA absorption model to the already attenuated continuum. From this exercise, we can only obtain the lower limit of the proximity zone size, i.e., $R_p \gtrsim 1.35$ pMpc, which corresponds to a quasar lifetime of $t_Q \gtrsim 10^{3.5}$ years. We caution that if the ionization bubble created by the quasar reaches the sub-DLA location and beyond but is hidden from the observer due to the blockage by the sub-DLA, the proximity zone size will no longer be sensitive to quasar age. Therefore, another independent diagnostic for a young quasar lifetime would be required.

We find such evidence based on the observed Ly α halo size of PSO J083+11 for this case. As a rough calculation, we estimate the size as the distance traveled by the light from the central accretion disk to the halo as $R_{\text{halo}} = c \times t$. Here, c is the light speed, and t is the light travel time. In Figure 5 we see the detection of halo within a $0''.6$ aperture radius, but then the fluxes are decreasing and hit the background level at around $1''$. In other words, the halo would have a minimum projected size of 3.32 pkpc with a maximum radial extent up to 5.54 pkpc, and there is no detection of extended Ly α emissions beyond this radius. For a halo with that size, this corresponds to a light travel time of $t \sim 10^4$ years, providing additional and independent evidence supporting the young quasar scenario for PSO J083+11. If the quasar has been accreting for a much longer period (i.e., $t_Q \gtrsim 10^5$ years), but its ionizing radiation could not be observed due to obscuration along our sightline, the Ly α halo around the quasar is likely to extend along the other unobscured sightlines (Farina et al. 2019; Eilers et al. 2021). For PSO J083+11, the aforementioned case

seems unlikely because we do not find any sign of extended Ly α emission. Contrastly, the Ly α ionized nebula is predicted to be modest or absent if the quasar’s radiation has only recently turned on (Eilers et al. 2018a).

As a side note, we attempted to look for the galaxy’s emission associated with the PSO J083+11’s sub-DLA using ALMA data (see Appendix D for details). A neighboring [C II] 158 μm emitter, J083.8372+11.8474, at $z = 6.3309$ is detected in the southwest direction from PSO J083+11, where the projected separation between them is $2''.88$ (~ 16 kpc). This source has an integrated [C II] flux of $0.61 \pm 0.01 \text{ Jy km s}^{-1}$, full width half at maximum (FWHM) of $318 \pm 58 \text{ km s}^{-1}$, and luminosity of $L_{[\text{CII}]} = 6.22 \pm 0.14 \times 10^8 L_{\odot}$. Its [C II] line properties are similar to those of $z \sim 4$ DLAs studied by Neeleman et al. (2019a) as well as companion galaxies around $z \gtrsim 6$ quasars (e.g., Neeleman et al. 2019b; Pensabene et al. 2021). However, the [C II]-based redshift of this PSO J083+11’s companion galaxy significantly differs from the sub-DLA’s redshift estimated via the centroids of rest-frame ultraviolet metal absorption lines. The velocity offset of $\Delta V = 692 \text{ km s}^{-1}$ between those two sources might indicate that they are two unrelated galaxies.

6. SUMMARY AND CONCLUSION

In this study, we characterized the environment and absorption systems toward PSO J083+11, a weak-line quasar at $z = 6.3401$. The strong Ly α absorption along with several metal lines (e.g., Mg II, O I, and C II) is observed in the Gemini/GNIRS, Magellan/FIRE, and VLT/MUSE spectra. This indicates the presence of a sub-DLA system at $z = 6.314$ and a strong Mg II absorber at $z = 2.2305$. To explain the detected Ly α damping wing, we model the corresponding absorption profile with a combination of a sub-DLA with a column density of neutral hydrogen of $\log N_{\text{HI}} = 20.03 \pm 0.30 \text{ cm}^{-2}$ plus absorption from an IGM with a neutral fraction of around 10%. The sub-DLA toward PSO J083+11 has an abundance ratio of $[\text{C}/\text{O}] = -0.04 \pm 0.33$ and metallicity of $[\text{O}/\text{H}] = -2.19 \pm 0.44$, similar to those of low-redshift metal-poor DLAs. The presence of this sub-DLA truncates PSO J083+11’s proximity zone and complicates the quasar lifetime measurement. However, at the same time, this quasar shows no sign of Ly α halo, where the estimated 1σ surface brightness limit is $2.76 \times 10^{-18} \text{ erg s}^{-1} \text{ cm}^{-2} \text{ arcsec}^{-2}$ at $1''$ aperture radius, or corresponds to Ly α luminosity of $\leq 43.46 \text{ erg s}^{-1}$. This non-detection provides an alternative and independent support for the young quasar hypothesis, where the unobscured accretion life-

time leads to small or no Ly α halo simply from a so-far limited light travel distance.

To obtain more evidence in the future, observations of extended narrow line emissions around PSO J083+11 might be needed. If this object is really in the early stage of quasar activation, the radial size of the extended narrow line region – which can be traced with [O III] λ 5007 or H α λ 6563 – would have to be small. This would require high sensitivity, high angular resolution mid-infrared observations with the James Webb Space Telescope. Building up a more coherent sample of young quasars with high black hole masses at this epoch will be the next step to understanding whether these are intermittent accretion phases in late-stage SMBH formation – or whether we are reaching the limit of observing the bulk of SMBH mass buildup through optical-NIR selection techniques, if most of SMBH occurs through obscured, possibly radiatively inefficient accretion modes.

As a very different aspect, one way to understand more about the epoch of reionization and the formation of the first galaxies is by studying the absorption systems toward the highest-redshift quasars. These systems, which at $2 \lesssim z \lesssim 4$ resemble present-day dwarf galaxies (Cooke et al. 2015), likely play a significant role in driving the reionization of the IGM, as predicted by numerical simulations. In just several hundred Myr after the Big Bang, they have experienced substantial enrichment of their gas while retaining a high neutral fraction, which provides an important clue about the contributing stellar populations. However, direct detections of these dwarfs will be tough even with the next-generation telescope. Therefore, “quasar absorption spectroscopy” is probably still the best way to study them in detail – and searching for and finding subsequently more and higher redshift DLAs will be powerful, though challenging, path to fully employ this technique.

1 We thank the anonymous referees for the constructive
2 comments on the manuscript. We would like to thank
3 Robert Simcoe for providing the codes for fitting the
4 metal absorption lines. I.T.A. would personally like to
5 thank Elsa P. Silfia for her incredible support and un-
6 ending encouragement, particularly in the most difficult
7 times.

8 This paper is based on observations collected at the
9 European Organisation for Astronomical Research in
10 the Southern Hemisphere under ESO program 0104.B-
11 0665(A). Part of the data presented in this paper is
12 based on observations obtained at the international
13 Gemini Observatory (GN-2019A-FT-204). Gemini Ob-
14 servatory is managed by the Association of Universities
15 for Research in Astronomy (AURA) under a coopera-
16 tive agreement with the National Science Foundation
17 on behalf of the Gemini Observatory partnership: the
18 National Science Foundation (United States), National
19 Research Council (Canada), Agencia Nacional de Inves-
20 tigación y Desarrollo (Chile), Ministerio de Ciencia, Tec-
21 nología e Innovación (Argentina), Ministério da Ciência,
22 Tecnologia, Inovações e Comunicações (Brazil), and Ko-
23 rea Astronomy and Space Science Institute (Republic of
24 Korea). This paper includes data gathered with FIRE at
25 6.5 m Magellan Baade Telescopes located at Las Cam-
26 panas Observatory. This paper makes use of the follow-
27 ing ALMA data: ADS/JAO.ALMA#2019.1.01436.S.
28 ALMA is a partnership of ESO (representing its member
29 states), NSF (USA), and NINS (Japan), together with
30 NRC (Canada), MOST and ASIAA (Taiwan), and KASI
31 (Republic of Korea), in cooperation with the Republic
32 of Chile. The Joint ALMA Observatory is operated by
33 ESO, AUI/NRAO, and NAOJ.

Facilities: VLT:Yepun (MUSE), Magellan:Baade
(FIRE), Gemini:Gillett (GNIRS)

Software: APLpy (Robitaille & Bressert 2012; Ro-
bitaille 2019), Astropy (Astropy Collaboration et al.
2013, 2018), CosmoCalc (Wright 2006), Linetools
(Prochaska et al. 2016), Lmfit (Newville et al. 2019),
Matplotlib (Caswell et al. 2019), NumPy (Harris et al.
2020), Pandas (Reback et al. 2021), Photutils (Bradley
et al. 2021), SciPy (Virtanen et al. 2020), Spectral-cube
(Robitaille et al. 2016), SpectRes (Carnall 2017)

APPENDIX

A. POSTERIOR DISTRIBUTIONS OF PARAMETERS

We show the posterior distributions of thermal parameter (T), turbulent parameter (b), and metal column densities in Figure 7. The inferred b seems biased toward large values while T is loosely constrained, probably because we only consider the absorption model with one velocity component. Metal absorbers at lower- z tend to show quiescent kinematics with $b \lesssim 30 \text{ km s}^{-1}$ (e.g., Cooper et al. 2019). It might be possible that the sub-DLA toward PSO J083+11 contains clouds with more than one velocity component. However, this is difficult to constrain using our current data due to spectral resolution limitations. Nevertheless, Simcoe et al. (2020) found that their code is robust enough for calculating the cumulative column density (N) in case of unresolved multiple narrow components, even though the N of the individual clouds is highly uncertain.

B. DAMPING WING MODELING USING MUSE AND FIRE SPECTRA

As mentioned in Section 3.2, we prefer to use the MUSE + GNIRS spectrum for modeling the intrinsic quasar spectrum because it has a better overall signal in the spectral data. Here, we attempt to use the MUSE and lower quality FIRE spectra for Ly α damping wing modeling as a comparison. PSO J083+11’s intrinsic emission was very difficult to be modeled using this dataset. As seen in Figure 8, there are spurious spikes in the spectrum – likely caused by imperfect telluric correction and hence spectrophotometric calibration at each wavelength due to low S/N – which make it nearly impossible for the PCA to anchor on relevant emission features. We had to extensively perturb the PCA fit to get a sensible solution that does not run into unphysical parameters. It turns out that PCA fit did not converge to a proper minimum within the physical parameter range. Despite the complications in modeling PSO J083+11’s intrinsic emission, we attempt to fit the Ly α absorption as explained in Section 3.2, using the nominal Ly α line prediction by the PCA model. These result in best-fit value of $\log N_{\text{HI}} = 20.23 \pm 0.30 \text{ cm}^{-2}$ for pure sub-DLA model and $\log N_{\text{HI}} = 19.66 \pm 0.30 \text{ cm}^{-2}$ for joint IGM + DLA model. However, the pure sub-DLA model systematically overestimates the fluxes around $\lambda = 1216\text{--}1225 \text{ \AA}$ (see Figure 9). In addition to that, the joint IGM + DLA model requires an IGM with hydrogen neutral fraction of $\bar{x}_{\text{HI}} = 0.8$, which seems to be substantially too high at $z \sim 6$ and contradicts measurements of prior

studies (e.g., Davies et al. 2018b; Bañados et al. 2019; Wang et al. 2020; Yang et al. 2020b). Consequently, we disregard this model to make any further quantitative statements.

C. EXPLORING THE EFFECT OF DIFFERENT IGM AND SUB-DLA CONTRIBUTIONS

In the main text (Section 3.2), we discussed how the profile of the damping wing in the PSO J083+11 spectrum could be produced by an accumulation of a proximate sub-DLA and a neutral intervening IGM. Here we explore how different combinations of those two parameters affect the quasar spectrum. In Figure 10 (see left panels) we present cases with neutral hydrogen fractions of $\bar{x}_{\text{HI}} = 0.0$ to 0.7 and how these values change the best-fit inferred neutral hydrogen column density of the sub-DLA from $\log N_{\text{HI}} = 20.11$ to 19.49 cm^{-2} . We also investigate the effect of the quasar’s proximity zone to the derived \bar{x}_{HI} and N_{HI} , if it extends beyond certain redshifts (see right panels). Following the formalism of Miralda-Escudé (1998), we tried to model the IGM damping wing presuming a constant neutral fraction from quasar’s proximity zone at redshift $z = z_s$ to $z = 5.5$, while being entirely ionized around $z \lesssim 5.5$. We find that values of the IGM neutral fraction $\bar{x}_{\text{HI}} > 0.5$ seem implausible because the best-fit damping wing profiles systematically do not match the observed fluxes around $\lambda = 1216\text{--}1225 \text{ \AA}$. On the other hand, the cases with $\bar{x}_{\text{HI}} \lesssim 0.5$ seem to produce comparably good fits to the data. In the end, we choose our preferred model as discussed in Section 3.2, i.e., a 10% neutral IGM and correspondingly a best-fit sub-DLA profile of $\log N_{\text{HI}} = 20.03 \pm 0.30 \text{ cm}^{-2}$. This value covers the best-fit N_{HI} values for all cases with $\bar{x}_{\text{HI}} \leq 50\%$.

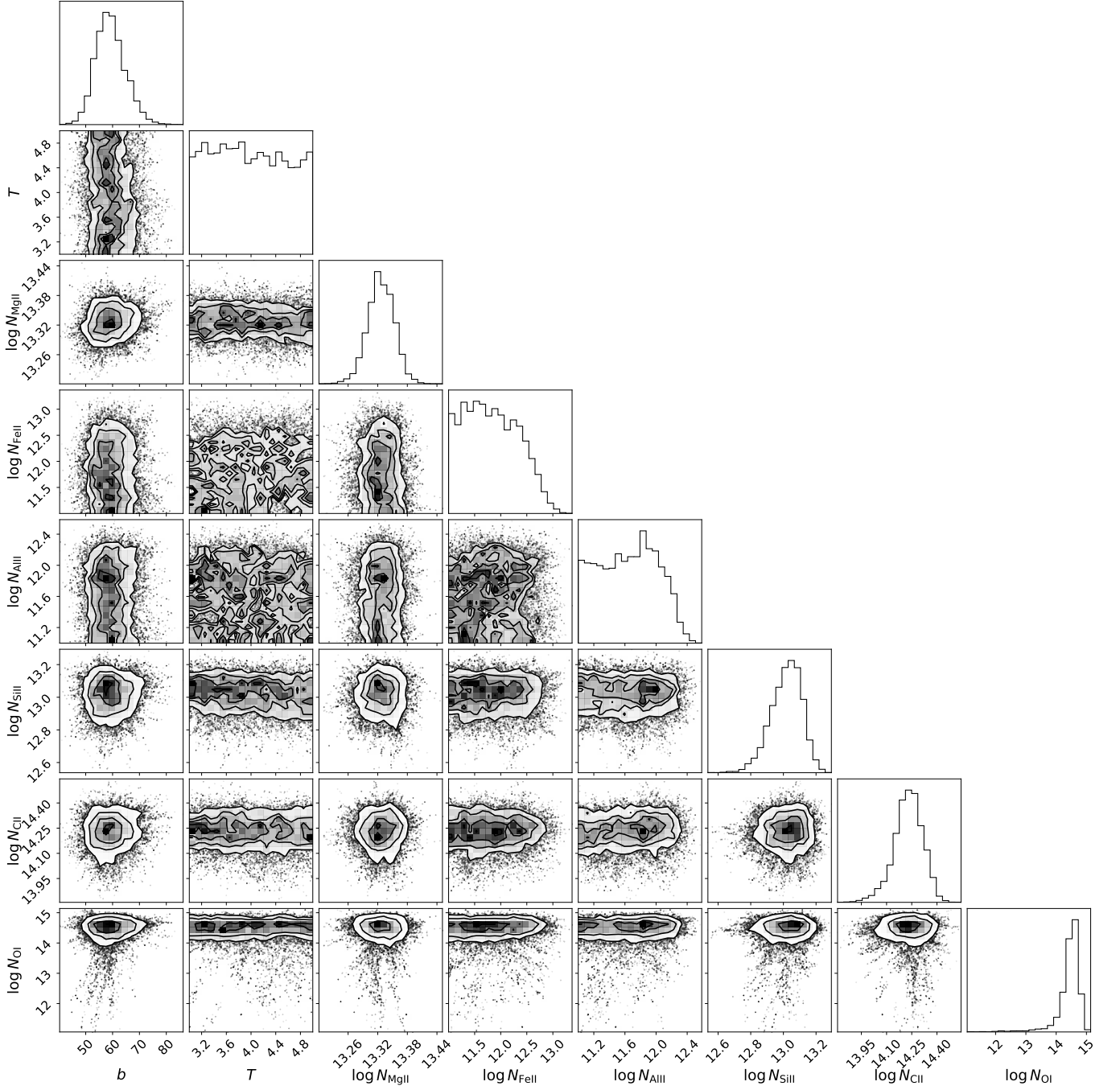


Figure 7. A corner plot showing posterior distributions of thermal parameter (T), turbulent parameter (b), and metal column densities listed in Table 1. The inferred b seems biased toward large values while T is highly uncertain (see text). The column densities of Mg II and C II are well constrained because they are clearly detected in the spectrum (see Figure 1). On the other hand, the marginal detection of O I makes its inferred column density has higher error. Non-detections are obvious for Al II and Fe II where their posteriors extend to the minimum value of input prior. We also adopt the upper limit value for Si II because its presence is not evident in the spectrum.

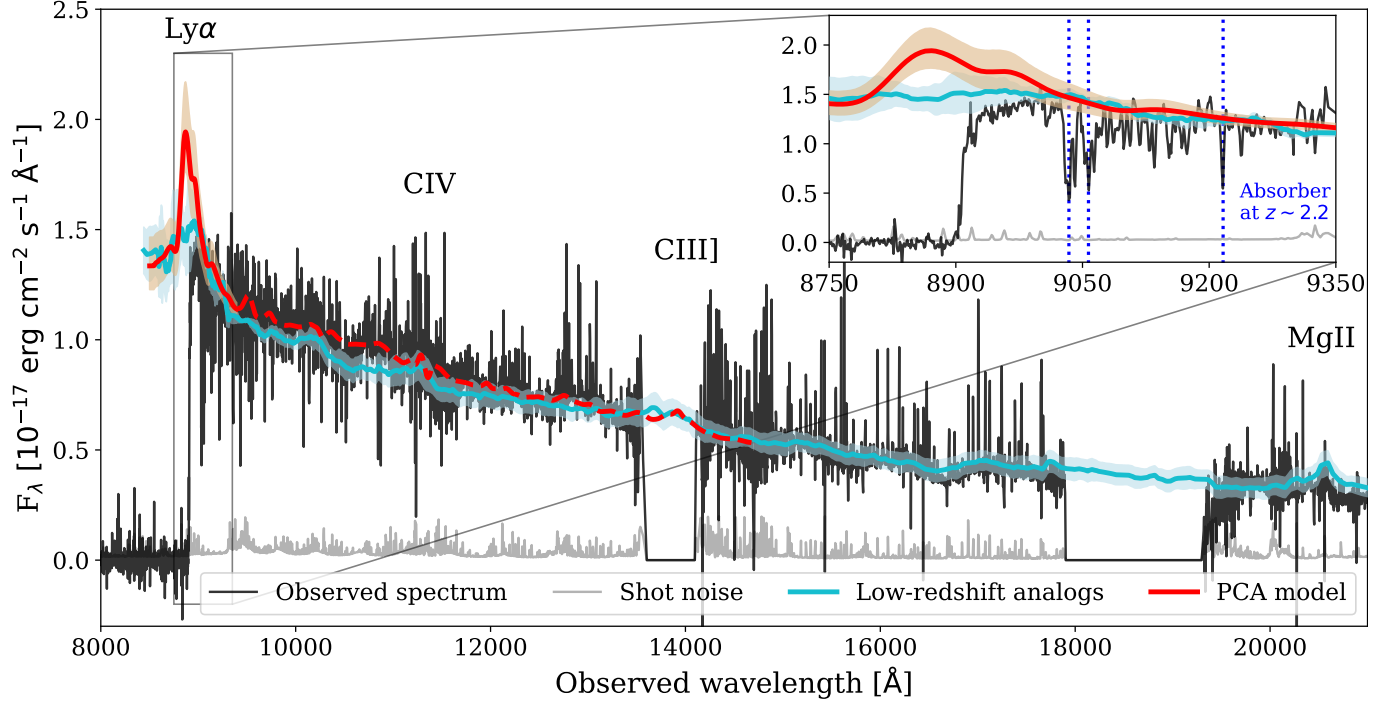


Figure 8. The MUSE + FIRE spectrum of PSO J083+11 (black line) and its associated shot noise (grey line). The median composite spectrum of the low-redshift quasar analogs is shown as a cyan line with the 1σ dispersion around the median as a light blue region. The PCA model to predict the blue-side of the quasar spectrum and its 1σ dispersion are denoted with the red line and shaded region, respectively. The wavelength range and spectrum used in the PCA fit to predict Ly α is shown with the red dashed line. The inset figure shows the zoom-in to the region around Ly α .

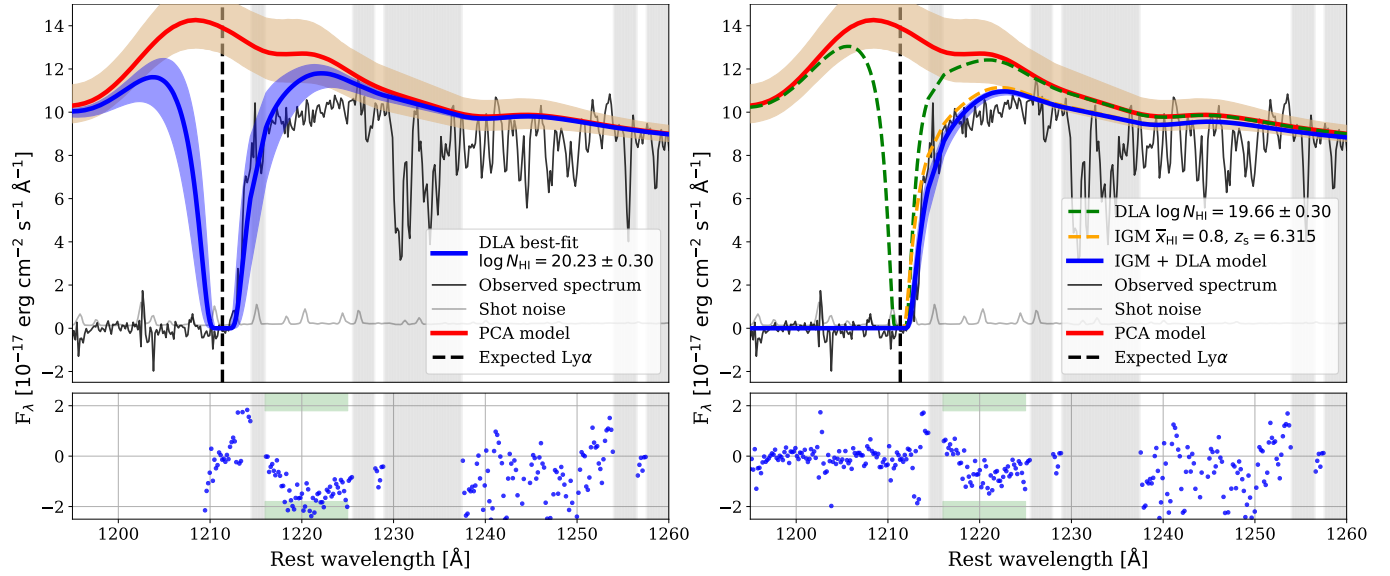


Figure 9. The MUSE + FIRE spectrum of PSO J083+11 (black line), shot noise (grey line), and the associated PCA model (red line and shaded region) around the wavelength region where the quasar’s Ly α emission is expected. The *left panel* shows the absorption from a $z = 6.314$ sub-DLA with a hydrogen column density of $\log N_{\text{HI}} = 20.23 \pm 0.30 \text{ cm}^{-2}$ (blue line and shaded region). The *right panel* presents a joint model where we incorporated attenuation due to an IGM with $\bar{x}_{\text{HI}} = 0.8$ (orange dashed line) and sub-DLA with $\log N_{\text{HI}} = 19.66 \pm 0.30 \text{ cm}^{-2}$ (green dashed line). This joint IGM + DLA model (blue line and shaded region) reconstructs the data at $\lambda = 1216\text{--}1225 \text{ \AA}$ better (see wavelengths marked with green), but it seems to be unphysical (see text). The residual of the fits (blue circles) and masked wavelengths to avoid strong absorption lines or regions with large uncertainty in the sky-subtraction (grey shaded area) are also presented in the figure.

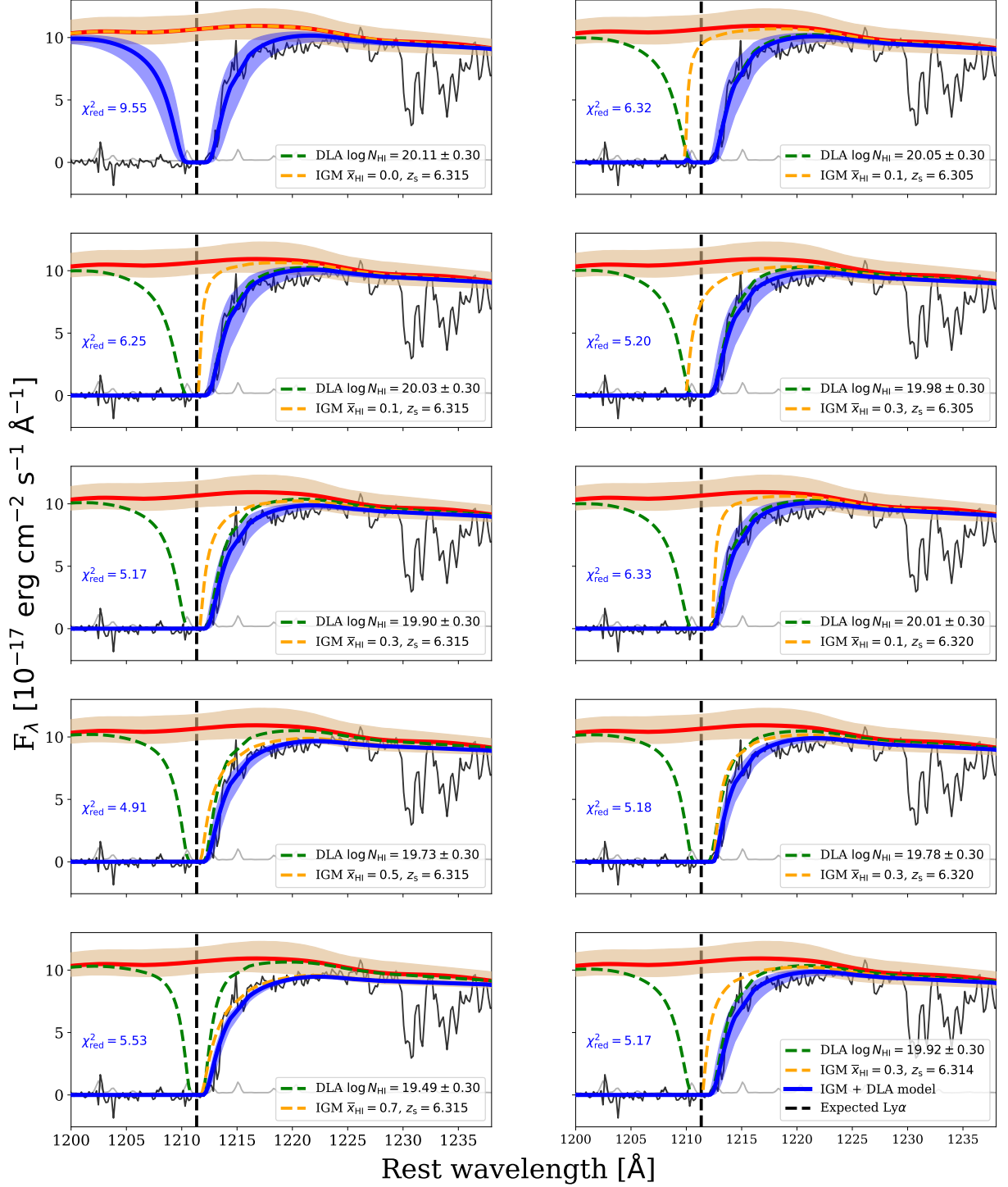


Figure 10. All panels show the observed spectrum of PSO J083+11 (solid black line), its 1σ shot noise vector (grey line), PCA continuum model (red line), and best-fit damping wing model (blue line). In the *top left panel*, we present the damping wing shape assuming there is zero IGM contribution (i.e., $\bar{x}_{\text{HI}} = 0.0$). The rest of the *left panels* present the increasing attenuation by the IGM with the sub-DLA Voigt profiles (green dashed lines, see legends) being modeled using the already attenuated quasar continuum (orange dashed lines) as input. The combination (blue line) is the best-fit match for the observed spectrum (solid black lines). The reduced chi-squared (χ^2_{red}) value for each IGM + DLA model is indicated with the blue text. As discussed in Section 3.2, the fiducial model that we choose is a 10% neutral IGM and correspondingly a best-fit sub-DLA profile of $\log N_{\text{HI}} = 20.03 \pm 0.30 \text{ cm}^{-2}$. The *right panels* show the example cases where the quasar’s proximity zones extend beyond or within the sub-DLA redshifts but still give comparably good fits.

D. SEARCHING FOR THE SUB-DLA HOST GALAXY'S EMISSION

Due to the intrinsic faintness of $z \gtrsim 2$ DLAs, finding the associated emission from their host galaxies is a challenging task (e.g., Kulkarni et al. 2006; Fumagalli et al. 2015). To date, there are a few tens of cases where those DLA host galaxies are successfully detected, either at optical/near-infrared or far-infrared wavelengths (e.g., Krogager et al. 2017; Fynbo et al. 2018; Kanekar et al. 2018; Møller et al. 2018; Klitsch et al. 2019; Neeleman et al. 2019a, 2020). In this section, we attempt to search for the galaxy's emission associated with the sub-DLA toward PSO J083+11 using Atacama Large Millimeter/submillimeter Array (ALMA; C43-4 array configuration) data taken by Andika et al. (2020). At $z \sim 6.3$, the [C II] 158 μm atomic fine-structure line is redshifted into the wavelengths covered by ALMA band-6, which is beneficial for identifying companion galaxy near PSO J083+11. We refer the reader to see Andika et al. (2020) for the details on the data reduction procedure. The final reduced datacube covers 257.5–261.1 GHz spectral window and has synthesized beam of $0''.42 \times 0''.37$, 30 MHz channel width, and root-mean-square (RMS) noise level of ~ 0.24 mJy beam $^{-1}$.

Through a visual inspection of the spectral channels, we detected emission of a companion galaxy, J083.8372+11.8474, in the southwest direction from PSO J083+11, with a projected angular distance of $2''.88$, or equivalent to a projected physical separation of ~ 16 kpc. To visualize it, we created a moment-zero map⁵ of [C II] 158 μm with a velocity width of 800 km s $^{-1}$ centered at $\nu_{\text{obs}} = 259.25$ GHz. The result is shown in the left panel of Figure 11, where we can see that the companion galaxy is observed as a marginally resolved single blob with a size of $0''.89 \times 0''.37$, or corresponds to a physical extent of 4.9 kpc \times 2.1 kpc at its redshift. The size above is equivalent to the major and minor axis full width at half maximums (FWHMs), calculated by fitting a 2D Gaussian function to the velocity-integrated [C II] map. After that, we extracted the spectrum around the companion galaxy location using a circular aperture with a radius of $1''$. This particular aperture size was selected because there is no apparent emission beyond this region. Aforementioned analysis led us to the discovery of a [C II] 158 μm emission at $z = 6.3309 \pm 0.0004$ with the observed frequency of $\nu_{\text{obs}} = 259.25 \pm 0.02$ GHz. Note that the underlying continuum emission is not detected, where the esti-

mated 3σ upper limit of flux density is 27.99 μJy for $1''$ aperture radius. By modeling the line with a 1D Gaussian function, we obtained an integrated [C II] flux of 0.61 ± 0.01 Jy km s $^{-1}$ and FWHM of 318 ± 58 km s $^{-1}$.

We subsequently calculate the [C II] line luminosity following Carilli & Walter (2013) prescription (see also Equation 15–16 in Andika et al. 2020), where the resulting value is $L_{[\text{CII}]} = 6.22 \pm 0.14 \times 10^8 L_{\odot}$. After that, the star formation rate (SFR) can be estimated employing the known SFR– $L_{[\text{CII}]}$ scaling relation for the high- z galaxies (De Looze et al. 2014), where we obtain SFR = $71 M_{\odot}$ yr $^{-1}$. It is also important to note that the relation above contains a systematic uncertainty of a factor of ~ 2.5 , which consequently makes the derived SFR has a range of 29–179 M_{\odot} yr $^{-1}$.

Previously, Neeleman et al. (2019a) reported [C II] emission from a sample of four DLAs at $z \sim 4$. Those DLA host galaxies have relatively large projected separation from the central quasar (16–45 kpc), luminosities of $L_{[\text{CII}]} = 0.36\text{--}30 \times 10^8 L_{\odot}$, and SFRs of 7–110 M_{\odot} yr $^{-1}$. The companion galaxy we found here has similar [C II] line properties as the aforementioned DLAs. However, the [C II]-based redshift of PSO J083+11's companion galaxy significantly differs from the sub-DLA's redshift ($z_{\text{DLA}} = 6.314$) estimated via the centroids of rest-frame ultraviolet metal absorption lines. The calculated velocity offset between those two sources is $\Delta V = 692$ km s $^{-1}$, or about two times the FWHM of [C II], which make them more likely to be two unrelated galaxies. So, we do not identify any emission by the sub-DLA host galaxy.

We were also not able to confidently identify the optical counterpart of J083.8372+11.8474. We searched by inspecting the MUSE image centered around PSO J083+11 with an overlay of [C II] emission from ALMA data (see Figure 12). We also extract the corresponding optical spectrum using an aperture with a $0''.5$ radius. There are no prominent emission lines detected around $\lambda_{\text{obs}} = 8839\text{--}8985$ Å, where the Ly α emission from PSO J083+11's companion galaxy is expected. The apparent faint continuum emission in the spectrum is most likely originated from the adjacent bright galaxy at $z \approx 0.29$.

⁵ For details on the equation used for computing moment map, see <https://spectral-cube.readthedocs.io/en/latest/moments.html>.

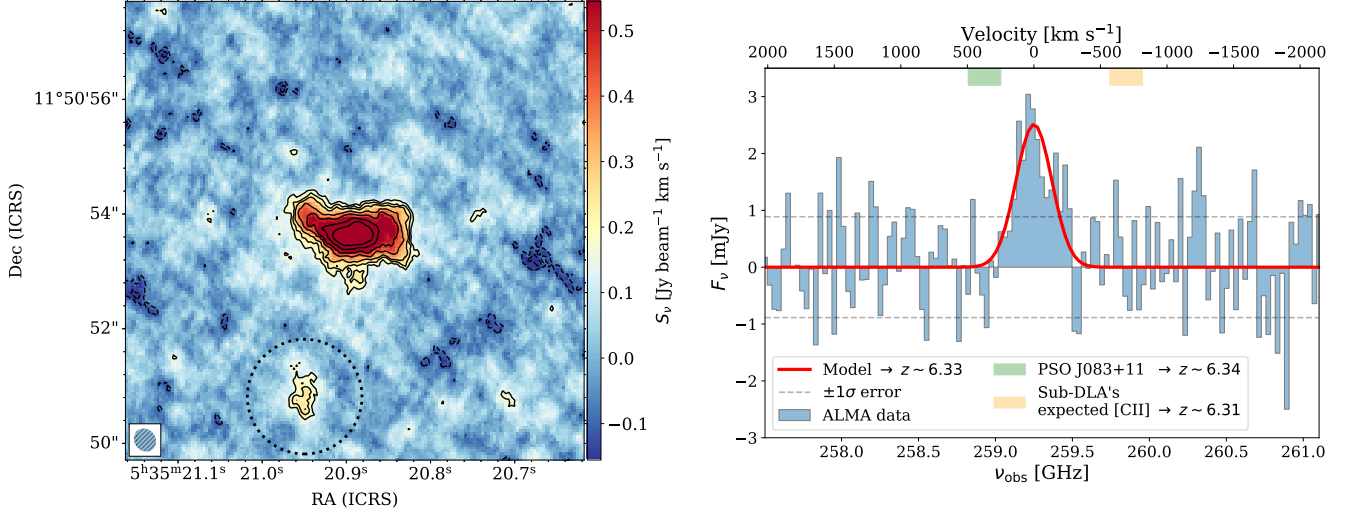


Figure 11. *Left panel:* The velocity-integrated [C II] map of the sky region around PSO J083+11. We find a companion galaxy in the southwest direction from the central quasar, with a projected angular separation of $2''.88$, or equivalent to ~ 16 kpc at $z = 6.3309$. The ALMA synthesized beam's size is presented at the bottom left. The solid black lines denote the [C II] velocity-integrated flux contours with $[3, 4, 5, 7, 9, 12, 15] \times \sigma$, where $\sigma = 0.053 \text{ Jy beam}^{-1} \text{ km s}^{-1}$. Contours with negative values are shown with dashed black lines. For extracting the spectrum and calculating the total [C II] flux density of the companion galaxy, we use a circular aperture (see dotted circles) with a radius of $1''$ (equivalent to 5.5 kpc). *Right panel:* The companion galaxy's [C II] emission at the observed frequency of $\nu_{\text{obs}} = 259.25 \text{ GHz}$. The observed flux density, its associated $\pm 1\sigma$ uncertainty, and the fitted Gaussian model are shown with the blue, dashed gray, and solid red lines, respectively. The velocity axis centered at $z = 6.3309$ is presented at the top. The expected central wavelengths of [C II] lines from the sub-DLA at $z = 6.314$ and PSO J083+11 at $z = 6.3401$ discussed in the main text are marked with the orange and green area, respectively.

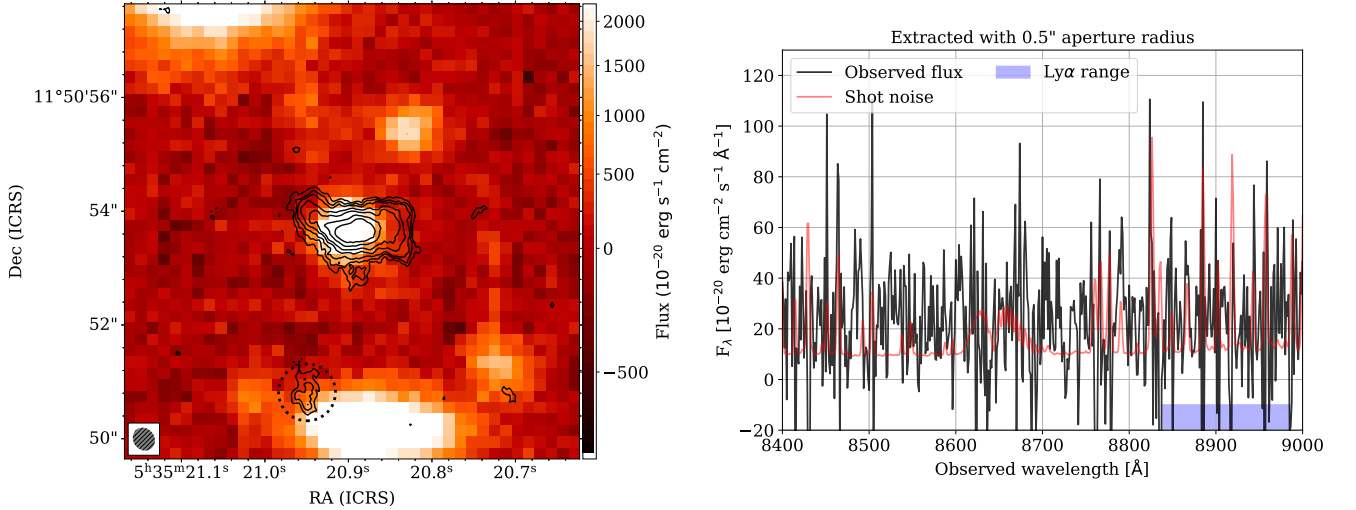


Figure 12. *Left panel:* The MUSE image centered around PSO J083+11, created by collapsing the $\lambda_{\text{obs}} = 8000\text{--}9000 \text{ \AA}$ layers. An overlay of [C II] emission from ALMA data is shown with a black contour. We then extract the spectrum at the region of interest using an aperture of $0''.5$ radius (dotted circles). *Right panel:* The MUSE spectrum of J083.8372+11.8474 (black line) – i.e., a $z = 6.3309$ companion galaxy near PSO J083+11 – and its associated shot noise (red line). We do not find any prominent emission lines in the wavelength region where the Ly α emission from the companion galaxy is expected (blue area). A faint continuum emission is seen, which originates from the adjacent bright galaxy at $z \approx 0.29$ in the southeast direction.

REFERENCES

- Abolfathi, B., Aguado, D. S., Aguilar, G., et al. 2018, *ApJS*, 235, 42, doi: [10.3847/1538-4365/aa9e8a](https://doi.org/10.3847/1538-4365/aa9e8a)
- Akerman, C. J., Carigi, L., Nissen, P. E., Pettini, M., & Asplund, M. 2004, *A&A*, 414, 931, doi: [10.1051/0004-6361:20034188](https://doi.org/10.1051/0004-6361:20034188)
- Andika, I. T., Jahnke, K., Onoue, M., et al. 2020, *ApJ*, 903, 34, doi: [10.3847/1538-4357/abb9a6](https://doi.org/10.3847/1538-4357/abb9a6)
- Arrigoni Battaia, F., Hennawi, J. F., Prochaska, J. X., et al. 2019, *MNRAS*, 482, 3162, doi: [10.1093/mnras/sty2827](https://doi.org/10.1093/mnras/sty2827)
- Asplund, M., Grevesse, N., Sauval, A. J., & Scott, P. 2009, *ARA&A*, 47, 481, doi: [10.1146/annurev.astro.46.060407.145222](https://doi.org/10.1146/annurev.astro.46.060407.145222)
- Astropy Collaboration, Robitaille, T. P., Tollerud, E. J., et al. 2013, *A&A*, 558, A33, doi: [10.1051/0004-6361/201322068](https://doi.org/10.1051/0004-6361/201322068)
- Astropy Collaboration, Price-Whelan, A. M., Sipőcz, B. M., et al. 2018, *AJ*, 156, 123, doi: [10.3847/1538-3881/aabc4f](https://doi.org/10.3847/1538-3881/aabc4f)
- Bañados, E., Venemans, B. P., Decarli, R., et al. 2016, *ApJS*, 227, 11, doi: [10.3847/0067-0049/227/1/11](https://doi.org/10.3847/0067-0049/227/1/11)
- Bañados, E., Venemans, B. P., Mazzucchelli, C., et al. 2018, *Nature*, 553, 473, doi: [10.1038/nature25180](https://doi.org/10.1038/nature25180)
- Bañados, E., Rauch, M., Decarli, R., et al. 2019, *ApJ*, 885, 59, doi: [10.3847/1538-4357/ab4129](https://doi.org/10.3847/1538-4357/ab4129)
- Begelman, M. C., Volonteri, M., & Rees, M. J. 2006, *MNRAS*, 370, 289, doi: [10.1111/j.1365-2966.2006.10467.x](https://doi.org/10.1111/j.1365-2966.2006.10467.x)
- Berg, T. A. M., Fumagalli, M., D’Odorico, V., et al. 2021, *MNRAS*, 502, 4009, doi: [10.1093/mnras/stab184](https://doi.org/10.1093/mnras/stab184)
- Bosman, S. E. I., Fan, X., Jiang, L., et al. 2018, *MNRAS*, 479, 1055, doi: [10.1093/mnras/sty1344](https://doi.org/10.1093/mnras/sty1344)
- Bosman, S. E. I., Ďurovčíková, D., Davies, F. B., & Eilers, A.-C. 2021a, *MNRAS*, 503, 2077, doi: [10.1093/mnras/stab572](https://doi.org/10.1093/mnras/stab572)
- Bosman, S. E. I., Davies, F. B., Becker, G. D., et al. 2021b, arXiv e-prints, arXiv:2108.03699, <https://arxiv.org/abs/2108.03699>
- Bradley, L., Sipőcz, B., Robitaille, T., et al. 2021, *astropy/photutils: 1.1.0, 1.1.0*, Zenodo, doi: [10.5281/zenodo.596036](https://doi.org/10.5281/zenodo.596036)
- Carilli, C. L., & Walter, F. 2013, *ARA&A*, 51, 105, doi: [10.1146/annurev-astro-082812-140953](https://doi.org/10.1146/annurev-astro-082812-140953)
- Carnall, A. C. 2017, arXiv e-prints, arXiv:1705.05165, <https://arxiv.org/abs/1705.05165>
- Caswell, T. A., Droettboom, M., Hunter, J., et al. 2019, *matplotlib/matplotlib v3.1.0, v3.1.0*, Zenodo, doi: [10.5281/zenodo.2893252](https://doi.org/10.5281/zenodo.2893252)
- Chambers, K. C., Magnier, E. A., Metcalfe, N., et al. 2016, arXiv e-prints, arXiv:1612.05560, <https://arxiv.org/abs/1612.05560>
- Chen, H., & Gnedin, N. Y. 2021, *ApJ*, 911, 60, doi: [10.3847/1538-4357/abe7e7](https://doi.org/10.3847/1538-4357/abe7e7)
- Cooke, R., Pettini, M., Steidel, C. C., Rudie, G. C., & Nissen, P. E. 2011, *MNRAS*, 417, 1534, doi: [10.1111/j.1365-2966.2011.19365.x](https://doi.org/10.1111/j.1365-2966.2011.19365.x)
- Cooke, R. J., Pettini, M., & Jorgenson, R. A. 2015, *ApJ*, 800, 12, doi: [10.1088/0004-637X/800/1/12](https://doi.org/10.1088/0004-637X/800/1/12)
- Cooke, R. J., Pettini, M., & Steidel, C. C. 2017, *MNRAS*, 467, 802, doi: [10.1093/mnras/stx037](https://doi.org/10.1093/mnras/stx037)
- Cooper, T. J., Simcoe, R. A., Cooksey, K. L., et al. 2019, *ApJ*, 882, 77, doi: [10.3847/1538-4357/ab3402](https://doi.org/10.3847/1538-4357/ab3402)
- Davies, F. B. 2020, *MNRAS*, 494, 2937, doi: [10.1093/mnras/staa528](https://doi.org/10.1093/mnras/staa528)
- Davies, F. B., Hennawi, J. F., & Eilers, A.-C. 2019, *ApJL*, 884, L19, doi: [10.3847/2041-8213/ab42e3](https://doi.org/10.3847/2041-8213/ab42e3)
- . 2020a, *MNRAS*, 493, 1330, doi: [10.1093/mnras/stz3303](https://doi.org/10.1093/mnras/stz3303)
- Davies, F. B., Wang, F., Eilers, A.-C., & Hennawi, J. F. 2020b, *ApJL*, 904, L32, doi: [10.3847/2041-8213/abc61f](https://doi.org/10.3847/2041-8213/abc61f)
- Davies, F. B., Hennawi, J. F., Bañados, E., et al. 2018a, *ApJ*, 864, 143, doi: [10.3847/1538-4357/aad7f8](https://doi.org/10.3847/1538-4357/aad7f8)
- . 2018b, *ApJ*, 864, 142, doi: [10.3847/1538-4357/aad6dc](https://doi.org/10.3847/1538-4357/aad6dc)
- Dayal, P., Rossi, E. M., Shiralilou, B., et al. 2019, *MNRAS*, 486, 2336, doi: [10.1093/mnras/stz897](https://doi.org/10.1093/mnras/stz897)
- De Looze, I., Cormier, D., Leboutteiller, V., et al. 2014, *A&A*, 568, A62, doi: [10.1051/0004-6361/201322489](https://doi.org/10.1051/0004-6361/201322489)
- D’Odorico, V., Feruglio, C., Ferrara, A., et al. 2018, *ApJL*, 863, L29, doi: [10.3847/2041-8213/aad7b7](https://doi.org/10.3847/2041-8213/aad7b7)
- Drake, A. B., Farina, E. P., Neeleman, M., et al. 2019, *ApJ*, 881, 131, doi: [10.3847/1538-4357/ab2984](https://doi.org/10.3847/1538-4357/ab2984)
- Eilers, A.-C., Davies, F. B., & Hennawi, J. F. 2018a, *ApJ*, 864, 53, doi: [10.3847/1538-4357/aad4fd](https://doi.org/10.3847/1538-4357/aad4fd)
- Eilers, A.-C., Davies, F. B., Hennawi, J. F., et al. 2017, *ApJ*, 840, 24, doi: [10.3847/1538-4357/aa6c60](https://doi.org/10.3847/1538-4357/aa6c60)
- Eilers, A.-C., Hennawi, J. F., & Davies, F. B. 2018b, *ApJ*, 867, 30, doi: [10.3847/1538-4357/aae081](https://doi.org/10.3847/1538-4357/aae081)
- Eilers, A.-C., Hennawi, J. F., Davies, F. B., & Simcoe, R. A. 2021, *ApJ*, 917, 38, doi: [10.3847/1538-4357/ac0a76](https://doi.org/10.3847/1538-4357/ac0a76)
- Eilers, A.-C., Hennawi, J. F., Decarli, R., et al. 2020, *ApJ*, 900, 37, doi: [10.3847/1538-4357/aba52e](https://doi.org/10.3847/1538-4357/aba52e)
- Fabbian, D., Nissen, P. E., Asplund, M., Pettini, M., & Akerman, C. 2009, *A&A*, 500, 1143, doi: [10.1051/0004-6361/200810095](https://doi.org/10.1051/0004-6361/200810095)
- Fan, X., Strauss, M. A., Becker, R. H., et al. 2006, *AJ*, 132, 117, doi: [10.1086/504836](https://doi.org/10.1086/504836)
- Farina, E. P., Venemans, B. P., Decarli, R., et al. 2017, *ApJ*, 848, 78, doi: [10.3847/1538-4357/aa8df4](https://doi.org/10.3847/1538-4357/aa8df4)
- Farina, E. P., Arrigoni-Battaia, F., Costa, T., et al. 2019, *ApJ*, 887, 196, doi: [10.3847/1538-4357/ab5847](https://doi.org/10.3847/1538-4357/ab5847)

- Ferrara, A., Salvadori, S., Yue, B., & Schleicher, D. 2014, *MNRAS*, 443, 2410, doi: [10.1093/mnras/stu1280](https://doi.org/10.1093/mnras/stu1280)
- Fischler, M. A., & Bolles, R. C. 1981, *Commun. ACM*, 24, 381–395, doi: [10.1145/358669.358692](https://doi.org/10.1145/358669.358692)
- Foreman-Mackey, D., Hogg, D. W., Lang, D., & Goodman, J. 2013, *PASP*, 125, 306, doi: [10.1086/670067](https://doi.org/10.1086/670067)
- Francis, P. J., Hewett, P. C., Foltz, C. B., & Chaffee, F. H. 1992, *ApJ*, 398, 476, doi: [10.1086/171870](https://doi.org/10.1086/171870)
- Fumagalli, M., O’Meara, J. M., Prochaska, J. X., Rafelski, M., & Kanekar, N. 2015, *MNRAS*, 446, 3178, doi: [10.1093/mnras/stu2325](https://doi.org/10.1093/mnras/stu2325)
- Fynbo, J. P. U., Heintz, K. E., Neeleman, M., et al. 2018, *MNRAS*, 479, 2126, doi: [10.1093/mnras/sty1520](https://doi.org/10.1093/mnras/sty1520)
- Gordon, K. D., Fouesneau, M., Arab, H., et al. 2016, *ApJ*, 826, 104, doi: [10.3847/0004-637X/826/2/104](https://doi.org/10.3847/0004-637X/826/2/104)
- Green, G. M., Schlafly, E., Zucker, C., Speagle, J. S., & Finkbeiner, D. 2019, *ApJ*, 887, 93, doi: [10.3847/1538-4357/ab5362](https://doi.org/10.3847/1538-4357/ab5362)
- Gunn, J. E., & Peterson, B. A. 1965, *ApJ*, 142, 1633, doi: [10.1086/148444](https://doi.org/10.1086/148444)
- Habouzit, M., Volonteri, M., Latif, M., Dubois, Y., & Peirani, S. 2016, *MNRAS*, 463, 529, doi: [10.1093/mnras/stw1924](https://doi.org/10.1093/mnras/stw1924)
- Harris, C. R., Millman, K. J., van der Walt, S. J., et al. 2020, *Nature*, 585, 357, doi: [10.1038/s41586-020-2649-2](https://doi.org/10.1038/s41586-020-2649-2)
- Inayoshi, K., Haiman, Z., & Ostriker, J. P. 2016, *MNRAS*, 459, 3738, doi: [10.1093/mnras/stw836](https://doi.org/10.1093/mnras/stw836)
- Kanekar, N., Prochaska, J. X., Christensen, L., et al. 2018, *ApJL*, 856, L23, doi: [10.3847/2041-8213/aab6ab](https://doi.org/10.3847/2041-8213/aab6ab)
- Kausch, W., Noll, S., Smette, A., et al. 2015, *A&A*, 576, A78, doi: [10.1051/0004-6361/201423909](https://doi.org/10.1051/0004-6361/201423909)
- Khrykin, I. S., Hennawi, J. F., Worseck, G., & Davies, F. B. 2021, *MNRAS*, 505, 649, doi: [10.1093/mnras/stab1288](https://doi.org/10.1093/mnras/stab1288)
- Klitsch, A., Zwaan, M. A., Péroux, C., et al. 2019, *MNRAS*, 482, L65, doi: [10.1093/mnrasl/sly187](https://doi.org/10.1093/mnrasl/sly187)
- Krogager, J. K., Møller, P., Fynbo, J. P. U., & Noterdaeme, P. 2017, *MNRAS*, 469, 2959, doi: [10.1093/mnras/stx1011](https://doi.org/10.1093/mnras/stx1011)
- Kulkarni, G., Hennawi, J. F., Rollinde, E., & Vangioni, E. 2014, *ApJ*, 787, 64, doi: [10.1088/0004-637X/787/1/64](https://doi.org/10.1088/0004-637X/787/1/64)
- Kulkarni, V. P., Woodgate, B. E., York, D. G., et al. 2006, *ApJ*, 636, 30, doi: [10.1086/497885](https://doi.org/10.1086/497885)
- Ma, Q., Maio, U., Ciardi, B., & Salvaterra, R. 2017, *MNRAS*, 472, 3532, doi: [10.1093/mnras/stx1839](https://doi.org/10.1093/mnras/stx1839)
- Mackenzie, R., Pezzulli, G., Cantalupo, S., et al. 2021, *MNRAS*, 502, 494, doi: [10.1093/mnras/staa3277](https://doi.org/10.1093/mnras/staa3277)
- Matsuoka, Y., Iwasawa, K., Onoue, M., et al. 2018, *ApJS*, 237, 5, doi: [10.3847/1538-4365/aac724](https://doi.org/10.3847/1538-4365/aac724)
- . 2022, *ApJS*, 259, 18, doi: [10.3847/1538-4365/ac3d31](https://doi.org/10.3847/1538-4365/ac3d31)
- Mazzucchelli, C., Bañados, E., Venemans, B. P., et al. 2017, *ApJ*, 849, 91, doi: [10.3847/1538-4357/aa9185](https://doi.org/10.3847/1538-4357/aa9185)
- Meyer, R. A., Bosman, S. E. I., & Ellis, R. S. 2019, *MNRAS*, 487, 3305, doi: [10.1093/mnras/stz1504](https://doi.org/10.1093/mnras/stz1504)
- Mignoli, M., Gilli, R., Decarli, R., et al. 2020, *A&A*, 642, L1, doi: [10.1051/0004-6361/202039045](https://doi.org/10.1051/0004-6361/202039045)
- Milutinovic, N., Ellison, S. L., Prochaska, J. X., & Tumlinson, J. 2010, *MNRAS*, 408, 2071, doi: [10.1111/j.1365-2966.2010.17280.x](https://doi.org/10.1111/j.1365-2966.2010.17280.x)
- Miralda-Escudé, J. 1998, *ApJ*, 501, 15, doi: [10.1086/305799](https://doi.org/10.1086/305799)
- Møller, P., Christensen, L., Zwaan, M. A., et al. 2018, *MNRAS*, 474, 4039, doi: [10.1093/mnras/stx2845](https://doi.org/10.1093/mnras/stx2845)
- Mortlock, D. J., Warren, S. J., Venemans, B. P., et al. 2011, *Nature*, 474, 616, doi: [10.1038/nature10159](https://doi.org/10.1038/nature10159)
- Morton, D. C. 2003, *ApJS*, 149, 205, doi: [10.1086/377639](https://doi.org/10.1086/377639)
- Neeleman, M., Kanekar, N., Prochaska, J. X., Rafelski, M. A., & Carilli, C. L. 2019a, *ApJL*, 870, L19, doi: [10.3847/2041-8213/aaf871](https://doi.org/10.3847/2041-8213/aaf871)
- Neeleman, M., Prochaska, J. X., Kanekar, N., & Rafelski, M. 2020, *Nature*, 581, 269, doi: [10.1038/s41586-020-2276-y](https://doi.org/10.1038/s41586-020-2276-y)
- Neeleman, M., Bañados, E., Walter, F., et al. 2019b, *ApJ*, 882, 10, doi: [10.3847/1538-4357/ab2ed3](https://doi.org/10.3847/1538-4357/ab2ed3)
- Newville, M., Otten, R., Nelson, A., et al. 2019, *lmfit/lmfit-py* 0.9.14, 0.9.14, Zenodo, doi: [10.5281/zenodo.3381550](https://doi.org/10.5281/zenodo.3381550)
- Nissen, P. E., Chen, Y. Q., Carigi, L., Schuster, W. J., & Zhao, G. 2014, *A&A*, 568, A25, doi: [10.1051/0004-6361/201424184](https://doi.org/10.1051/0004-6361/201424184)
- Ohsuga, K., Mori, M., Nakamoto, T., & Mineshige, S. 2005, *ApJ*, 628, 368, doi: [10.1086/430728](https://doi.org/10.1086/430728)
- Pacucci, F., & Loeb, A. 2022, *MNRAS*, 509, 1885, doi: [10.1093/mnras/stab3071](https://doi.org/10.1093/mnras/stab3071)
- Pâris, I., Petitjean, P., Rollinde, E., et al. 2011, *A&A*, 530, A50, doi: [10.1051/0004-6361/201016233](https://doi.org/10.1051/0004-6361/201016233)
- Pâris, I., Petitjean, P., Aubourg, É., et al. 2018, *A&A*, 613, A51, doi: [10.1051/0004-6361/201732445](https://doi.org/10.1051/0004-6361/201732445)
- Pensabene, A., Decarli, R., Bañados, E., et al. 2021, *A&A*, 652, A66, doi: [10.1051/0004-6361/202039696](https://doi.org/10.1051/0004-6361/202039696)
- Pons, E., McMahon, R. G., Simcoe, R. A., et al. 2019, *MNRAS*, 484, 5142, doi: [10.1093/mnras/stz292](https://doi.org/10.1093/mnras/stz292)
- Prochaska, J., Hennawi, J., Westfall, K., et al. 2020, *The Journal of Open Source Software*, 5, 2308, doi: [10.21105/joss.02308](https://doi.org/10.21105/joss.02308)
- Prochaska, J. X., Tejos, N., Crighton, N., et al. 2016, *Linetools/Linetools: Second Major Release, v0.2*, Zenodo, doi: [10.5281/zenodo.168270](https://doi.org/10.5281/zenodo.168270)
- Quiret, S., Péroux, C., Zafar, T., et al. 2016, *MNRAS*, 458, 4074, doi: [10.1093/mnras/stw524](https://doi.org/10.1093/mnras/stw524)
- Reback, J., Jbrockmendel, McKinney, W., et al. 2021, *pandas-dev/pandas: Pandas 1.3.0, v1.3.0*, Zenodo, doi: [10.5281/zenodo.3509134](https://doi.org/10.5281/zenodo.3509134)

- Reed, S. L., Banerji, M., Becker, G. D., et al. 2019, *MNRAS*, 487, 1874, doi: [10.1093/mnras/stz1341](https://doi.org/10.1093/mnras/stz1341)
- Robitaille, T. 2019, APLpy v2.0: The Astronomical Plotting Library in Python, doi: [10.5281/zenodo.2567476](https://doi.org/10.5281/zenodo.2567476)
- Robitaille, T., & Bressert, E. 2012, APLpy: Astronomical Plotting Library in Python, Astrophysics Source Code Library. <http://ascl.net/1208.017>
- Robitaille, T., Ginsburg, A., Beaumont, C., Leroy, A., & Rosolowsky, E. 2016, spectral-cube: Read and analyze astrophysical spectral data cubes. <http://ascl.net/1609.017>
- Schauer, A. T. P., Regan, J., Glover, S. C. O., & Klessen, R. S. 2017, *MNRAS*, 471, 4878, doi: [10.1093/mnras/stx1915](https://doi.org/10.1093/mnras/stx1915)
- Schindler, J.-T., Farina, E. P., Bañados, E., et al. 2020, *ApJ*, 905, 51, doi: [10.3847/1538-4357/abc2d7](https://doi.org/10.3847/1538-4357/abc2d7)
- Shen, Y., Richards, G. T., Strauss, M. A., et al. 2011, *ApJS*, 194, 45, doi: [10.1088/0067-0049/194/2/45](https://doi.org/10.1088/0067-0049/194/2/45)
- Shen, Y., Wu, J., Jiang, L., et al. 2019, *ApJ*, 873, 35, doi: [10.3847/1538-4357/ab03d9](https://doi.org/10.3847/1538-4357/ab03d9)
- Simcoe, R. A., Onoue, M., Eilers, A.-C., et al. 2020, arXiv e-prints, arXiv:2011.10582. <https://arxiv.org/abs/2011.10582>
- Simcoe, R. A., Burgasser, A. J., Schechter, P. L., et al. 2013, *PASP*, 125, 270, doi: [10.1086/670241](https://doi.org/10.1086/670241)
- Smette, A., Sana, H., Noll, S., et al. 2015, *A&A*, 576, A77, doi: [10.1051/0004-6361/201423932](https://doi.org/10.1051/0004-6361/201423932)
- Soto, K. T., Lilly, S. J., Bacon, R., Richard, J., & Conseil, S. 2016, *MNRAS*, 458, 3210, doi: [10.1093/mnras/stw474](https://doi.org/10.1093/mnras/stw474)
- Suzuki, N. 2006, *ApJS*, 163, 110, doi: [10.1086/499272](https://doi.org/10.1086/499272)
- Tanaka, T., & Haiman, Z. 2009, *ApJ*, 696, 1798, doi: [10.1088/0004-637X/696/2/1798](https://doi.org/10.1088/0004-637X/696/2/1798)
- Trakhtenbrot, B., Volonteri, M., & Natarajan, P. 2017, *ApJL*, 836, L1, doi: [10.3847/2041-8213/836/1/L1](https://doi.org/10.3847/2041-8213/836/1/L1)
- Ďurovčiková, D., Katz, H., Bosman, S. E. I., et al. 2020, *MNRAS*, 493, 4256, doi: [10.1093/mnras/staa505](https://doi.org/10.1093/mnras/staa505)
- Venemans, B. P., Bañados, E., Decarli, R., et al. 2015, *ApJL*, 801, L11, doi: [10.1088/2041-8205/801/1/L11](https://doi.org/10.1088/2041-8205/801/1/L11)
- Virtanen, P., Gommers, R., Oliphant, T. E., et al. 2020, *Nature Methods*, 17, 261, doi: <https://doi.org/10.1038/s41592-019-0686-2>
- Wang, F., Yang, J., Fan, X., et al. 2019, *ApJ*, 884, 30, doi: [10.3847/1538-4357/ab2be5](https://doi.org/10.3847/1538-4357/ab2be5)
- Wang, F., Davies, F. B., Yang, J., et al. 2020, *ApJ*, 896, 23, doi: [10.3847/1538-4357/ab8c45](https://doi.org/10.3847/1538-4357/ab8c45)
- Wang, F., Yang, J., Fan, X., et al. 2021, *ApJL*, 907, L1, doi: [10.3847/2041-8213/abd8c6](https://doi.org/10.3847/2041-8213/abd8c6)
- Weilbacher, P. M., Streicher, O., Urrutia, T., et al. 2012, in Society of Photo-Optical Instrumentation Engineers (SPIE) Conference Series, Vol. 8451, Software and Cyberinfrastructure for Astronomy II, ed. N. M. Radziwill & G. Chiozzi, 84510B, doi: [10.1117/12.925114](https://doi.org/10.1117/12.925114)
- Weilbacher, P. M., Streicher, O., Urrutia, T., et al. 2014, in Astronomical Society of the Pacific Conference Series, Vol. 485, Astronomical Data Analysis Software and Systems XXIII, ed. N. Manset & P. Forshay, 451. <https://arxiv.org/abs/1507.00034>
- Willott, C. J., Delorme, P., Reylé, C., et al. 2010, *AJ*, 139, 906, doi: [10.1088/0004-6256/139/3/906](https://doi.org/10.1088/0004-6256/139/3/906)
- Wolfe, A. M., Gawiser, E., & Prochaska, J. X. 2005, *ARA&A*, 43, 861, doi: [10.1146/annurev.astro.42.053102.133950](https://doi.org/10.1146/annurev.astro.42.053102.133950)
- Worseck, G., Khrykin, I. S., Hennawi, J. F., Prochaska, J. X., & Farina, E. P. 2021, *MNRAS*, 505, 5084, doi: [10.1093/mnras/stab1685](https://doi.org/10.1093/mnras/stab1685)
- Wright, E. L. 2006, *PASP*, 118, 1711, doi: [10.1086/510102](https://doi.org/10.1086/510102)
- Yang, J., Wang, F., Fan, X., et al. 2019, *AJ*, 157, 236, doi: [10.3847/1538-3881/ab1be1](https://doi.org/10.3847/1538-3881/ab1be1)
- . 2020a, *ApJL*, 897, L14, doi: [10.3847/2041-8213/ab9c26](https://doi.org/10.3847/2041-8213/ab9c26)
- . 2020b, *ApJ*, 904, 26, doi: [10.3847/1538-4357/abbc1b](https://doi.org/10.3847/1538-4357/abbc1b)
- Yip, C. W., Connolly, A. J., Vanden Berk, D. E., et al. 2004, *AJ*, 128, 2603, doi: [10.1086/425626](https://doi.org/10.1086/425626)